DRAFT VERSION FEBRUARY 17, 2022
Typeset using LaTeX **twocolumn** style in AASTeX62

The Metallicity Dependence of the High-Mass X-ray Binary Luminosity Function

BRET D. LEHMER,[1] RAFAEL T. EUFRASIO,[1] ANTARA BASU-ZYCH,[2,3] KEITH DOORE,[1] TASSOS FRAGOS,[4] KRISTEN GAROFALI,[1,2] KONSTANTINOS KOVLAKAS,[5,6] BENJAMIN F. WILLIAMS,[7] ANDREAS ZEZAS,[8,9,10] AND LUIDHY SANTANA-SILVA[11]

[1]*Department of Physics, University of Arkansas, 226 Physics Building, 825 West Dickson Street, Fayetteville, AR 72701, USA*
[2]*NASA Goddard Space Flight Center, Code 662, Greenbelt, MD 20771, USA*
[3]*Center for Space Science and Technology, University of Maryland Baltimore County, 1000 Hilltop Circle, Baltimore, MD 21250, USA*
[4]*Geneva Observatory, University of Geneva, Chemin des Maillettes 51, 1290 Sauverny, Switzerland*
[5]*Physics Department, University of Crete, GR 71003, Heraklion, Greece*
[6]*Institute of Astrophysics, Foundation for Research and Technology-Hellas, GR 71110 Heraklion, Greece*
[7]*Department of Astronomy, Box 351580, University of Washington, Seattle, WA 98195, USA*
[8]*Harvard-Smithsonian Center for Astrophysics, 60 Garden Street, Cambridge, MA 02138, USA*
[9]*Foundation for Research and Technology-Hellas, 100 Nikolaou Plastira Street, 71110 Heraklion, Crete, Greece*
[10]*Physics Department & Institute of Theoretical & Computational Physics, P.O. Box 2208, 71003 Heraklion, Crete, Greece*
[11]*NAT-Universidade Cruzeiro do Sul / Universidade Cidade de São Paulo, Rua Galvão Bueno, 868, 01506-000, São Paulo, SP, Brazil*

ABSTRACT

We present detailed constraints on the metallicity dependence of the high mass X-ray binary (HMXB) X-ray luminosity function (XLF). We analyze ≈5 Ms of *Chandra* data for 55 actively star-forming galaxies at $D \lesssim 30$ Mpc with gas-phase metallicities spanning $12+\log(\mathrm{O/H}) \approx 7$–9.2. Within the galactic footprints, our sample contains a total of 1311 X-ray point sources, of which ≈49% are expected to be HMXBs, with the remaining sources likely to be low-mass X-ray binaries (LMXBs; ≈22%) and unrelated background sources (≈29%). We construct a model that successfully characterizes the average HMXB XLF over the full metallicity range. We demonstrate that the SFR-normalized HMXB XLF shows clear trends with metallicity, with steadily increasing numbers of luminous and ultraluminous X-ray sources ($\log L(\mathrm{erg\ s^{-1}}) = 38$–40.5) with declining metallicity. However, we find that the low-luminosity ($\log L(\mathrm{erg\ s^{-1}}) = 36$–38) HMXB XLF appears to show a nearly constant SFR scaling and slope with metallicity. Our model provides a revised scaling relation of integrated L_X/SFR versus $12+\log(\mathrm{O/H})$ and a new characterization of its the SFR-dependent stochastic scatter. The general trend of this relation is broadly consistent with past studies based on integrated galaxy emission; however, our model suggests that this relation is driven primarily by the high-luminosity end of the HMXB XLF. Our results have implications for binary population synthesis models, the nature of super-Eddington accreting objects (e.g., ultraluminous X-ray sources), recent efforts to identify active galactic nucleus candidates in dwarf galaxies, and the X-ray radiation fields in the early Universe during the epoch of cosmic heating at $z \gtrsim 10$.

Keywords: stars: formation — galaxies: normal — X-rays: binaries — X-rays: galaxies

1. INTRODUCTION

Over the last ≈20 years, the *Chandra X-ray Observatory* (*Chandra*) has accumulated an extensive archive of X-ray imaging data capable of resolving populations of X-ray binaries (XRBs) within relatively nearby galaxies ($\lesssim 100$ Mpc). Thanks to these *Chandra* data, along with complementary multiwavelength data (e.g., from *GALEX*, *Spitzer*, *WISE*, and SDSS), it is now possible to conduct detailed statistically meaningful studies that characterize how the XRB X-ray luminosity functions (XLFs) vary with local physical properties (e.g., star-formation rate (SFR) and stellar mass ($M_\star$)). Such XRB XLF scaling relations provide important benchmarks for understanding X-ray emission from a variety of galaxy populations, compact object formation and evolution, the binary phase of stellar evolution, and several close-binary subclasses (e.g., gravitational-wave sources, short gamma-ray bursts, and millisecond pulsars).

On the observational side, XRB scaling relations are routinely used in assessing whether X-ray detected sources are consistent with stellar-mass XRBs or accreting supermassive black holes (SMBHs; see Mezcua et al. 2018, Latimer et al.

Corresponding author: Bret Lehmer
lehmer@uark.edu

2019, Birchall et al. 2020, Hodges-Kluck et al. 2020, Koudmani et al. 2020, and Secrest et al. 2020 for recent examples). These assessments are often based on XLF-integrated scaling relations and their galaxy-population statistical scatters (e.g., the L_X-SFR relation; Ranalli et al. 2003; Colbert et al. 2004; Persic & Rephaeli 2007; Lehmer et al. 2008, 2010, 2016, 2019, 2020; Mineo et al. 2012a, 2012b; Basu-Zych et al. 2013a; Aird et al. 2017). However, due to the often poor sampling of the bright-source ends of XLFs, these relations are likely to become non-linear with highly-skewed scatter distributions in the low-SFR and low-$M_\star$ regimes where they are often applied (e.g., Gilfanov et al. 2004; Justham & Schawinski 2012; Lehmer et al. 2019). A detailed characterization of how the XRB XLF varies with galaxy physical properties can provide appropriate statistical quantification of how X-ray scaling relations and their scatter vary across these properties.

Thus far, most XRB XLF scaling relation studies have focused on constraining the high-mass XRB (HMXB) and low-mass XRB (LMXB) XLF scalings with SFR and $M_\star$, respectively (e.g., Grimm et al. 2002; Gilfanov 2004; Mineo et al. 2012a; Zhang et al. 2012; Lehmer et al. 2019, 2020). However, recently it has become clear, from both theoretical and observational studies of integrated scaling relations, that additional physical parameters, including star-formation history (SFH) and metallicity, have important impacts on these scaling relations (e.g., Dray 2006; Mapelli et al. 2010; Kaaret et al. 2011; Basu-Zych et al. 2013b, 2016; Fragos et al. 2013a,b; Brorby et al. 2014, 2016; Douna et al. 2015; Lehmer et al. 2017; Antoniou et al. 2019; Fornasini et al. 2019, 2020; Kouroumpatzakis et al. 2020; Kovlakas et al. 2020).

Particular attention has been directed to the metallicity dependence of the HMXB XLF. HMXBs are the most luminous XRB population per stellar mass, and are expected to provide important ionizing radiation from stellar populations that both lasts longer than the far-UV emission from young massive stars and traverses longer path lengths before being absorbed. Given these properties, HMXBs have been proposed to play roles in (1) interstellar medium feedback (e.g., Pakull et al. 2010; Soria et al. 2010, 2014; Justham & Schawinski 2012; López et al. 2019); (2) the production of Lyman continuum radiation, as well as He II and Lyman-α emission lines from starbursts (e.g., Kaaret et al. 2017a; Bleum et al. 2019; Schaerer et al. 2019; Svoboda et al. 2019; Dittenber et al. 2020; Saxena et al. 2020; Senchyna et al. 2020); and (3) the heating of the early intergalactic medium at $z \gtrsim 10$ (e.g., Mirabel et al. 2011; Mesinger et al. 2013; Pacucci et al. 2014; Madau & Fragos 2017; Das et al. 2017; Greig & Mesinger 2018; Park et al. 2018; Heneka & Mesinger 2020).

While some basic models have been proposed for the HMXB XLF dependendence on metallicity (e.g., Brorby et al. 2014; Basu-Zych et al. 2016; Ponnada et al. 2020), these models are primarily based on interpreting the L_X/SFR versus metallicity relation (hereafter, the L_X–SFR–Z relation) in terms of a varying HMXB XLF normalization and power-law slope. Furthermore, studies that place direct constraints on the metallicity-dependence of point-source populations within galaxies have focused primarily on the ultraluminous X-ray source (ULX; $L > 10^{39}$ erg s^{-1}) formation rate per unit SFR (e.g., Zampieri & Roberts 2009; Mapelli et al. 2010; Prestwich et al. 2013; Douna et al. 2015; Kovlakas et al. 2020). These studies find a clear decline in the ULX rate with increasing metallicity; however, they do not characterize the luminosity dependence of this trend nor do they make a direct connection with more typical lower-luminosity XRB populations.

In a recent study of the XLFs of 38 nearby ($D < 30$ Mpc) galaxies (primarily late-type galaxies), Lehmer et al. (2019; hereafter, L19), we showed that the five lowest metallicity galaxies in the sample hosted a factor of $\approx$2–10 times excess of HMXBs with $L \gtrsim 5 \times 10^{38}$ erg s^{-1} compared to the average galaxy population, while the number of $L \approx$ (0.1–5) $\times 10^{38}$ erg s^{-1} sources in these relatively low-metallicity galaxies appeared to be consistent with the full galaxy sample. This suggests that the metallicity-dependent XLF evolution is more complex than a simple scaling in the overall normalization and power-law slope of the XLF.

In this paper, we expand on the early results from L19 and more fully characterize how the SFR-scaled HMXB XLF normalization and detailed shape vary with metallicity. In Section 2, we discuss our galaxy sample selection and present the galaxy properties. In Section 3, we briefly summarize our *Chandra* data analysis procedure, which follows closely the approach outlined in L19. In Section 4, we present our global metallicity-dependent HMXB XLF model and fitting results. In Section 5, we discuss our results in the context of past studies and highlight problems to address in future studies. Finally, Section 6 provides a summary of the key results from this work.

Unless noted otherwise, we make use of multiwavelength fluxes and luminosities that have been corrected for Galactic absorption, but not intrinsic absorption. Throughout, we quote X-ray luminosities in the 0.5–8 keV bandpass and use L to denote individual point-source luminosities and L_X to represent population-integrated luminosities. For clearer comparisons with past studies, we often quote SFR and $M_\star$ values that are based on a Kroupa (2001) initial mass function (IMF) at solar abundances, with a SFH that is constant over 13.6 Gyr. As we discuss in Section 2, the assumption of a constant abundance for these calculations has only a minor impact on our results.

2. SAMPLE SELECTION AND PROPERTIES

Given our goal to study the effects of metallicity on HMXB formation, we constructed relatively nearby ($D < 30$ Mpc) samples of star-forming galaxies with high specific SFRs (sSFR $\equiv$ SFR/$M_\star \gtrsim 10^{-10}$ yr^{-1}) that span a broad range of metallicity ($12+\log(\mathrm{O/H}) \approx$ 7–9.2; $Z \approx 0.02$–$3\ Z_\odot$).[1] The adopted sSFR boundary limits contributions from LMXBs that can dominate in lower sSFR galaxies (e.g., Lehmer et al. 2010; Kouroumpatzakis et al. 2020). We first assembled a *main sample* of 33 such objects that had both *Chandra* archival data from the literature and a suite of multi-wavelength observations spanning the UV to mid-IR. Our main sample contains (1) 23 galaxies from the spectroscopic study from Moustakas et al. (2010) of galaxies in the *Spitzer* Infrared Nearby Galaxies Survey (SINGS; Kennicutt et al. 2003); (2) six objects from Engelbracht et al. (2008); and (3) four additional nearby galaxies (NGC 5253, M83, M101, and DDO68) with deep *Chandra* exposures (>100 ks). We chose not to include well-studied disk-dominated galaxies with high inclination angles to our line of sight ($\gtrsim 70$ deg; e.g., M82 and NGC 253), due to highly varied (and occasionally very large) absorption of X-ray point-sources through the galactic disks.

In addition to our main sample, we assembled a *supplemental sample* of 22 extremely metal poor objects with $12+\log(\mathrm{O/H}) < 8$ and $D < 30$ Mpc that were drawn from Prestwich et al. (2013). We note that these galaxies have been utilized in the Brorby et al. (2014) and Douna et al. (2015) studies of X-ray properties of extremely metal-poor galaxies and include many of the lowest metallicity galaxies known in the local Universe. Galaxies in the supplementary sample are compact (≈0.″4–1.″4 semi-major axes) dwarf galaxies, and have relatively shallow *Chandra* and multiwavelength data compared to our main sample. Therefore, physical parameters are more uncertain for this population and X-ray constraints are limited to only bright point sources in the galaxies, with some uncertainty on whether they are XRB or SMBH dominated.

All galaxies in our samples have oxygen abundance measurements available from either strong-line calibrations or a "direct," electron-temperature-based theoretical calibration. The strong-line estimates were originally based on either the theoretical Kobulnicky & Kewley (2004; herafter, KK04) or empirical Pettini & Pagel (2004; PP04) calibrations. KK04 estimates were available for the 23 SINGS galaxies in our main sample via Moustakas et al. (2010), who utilized the R_{23} emission-line ratio, R_{23} = ([O II]λ3727 + [O III]$\lambda\lambda$4959, 5007)/Hβ, and [O III]λ5007/[O II]λ3727. PP04 estimates were available for M83 and M101 (Bresolin et al. 2009 and Hu et al. 2018), and are based on the ratio ([O III]λ5007/Hβ)/([N II]λ6584/Hα). All other galaxies, including eight main-sample galaxies ($12+\log(\mathrm{O/H}) \lesssim 8.4$), as well as the 22 extremely metal-poor supplemental-sample galaxies, had estimates based on the direct method (see Table 1 for references), which uses the [O III]$\lambda\lambda$4959, 5003/[O III]λ4363 ratio.

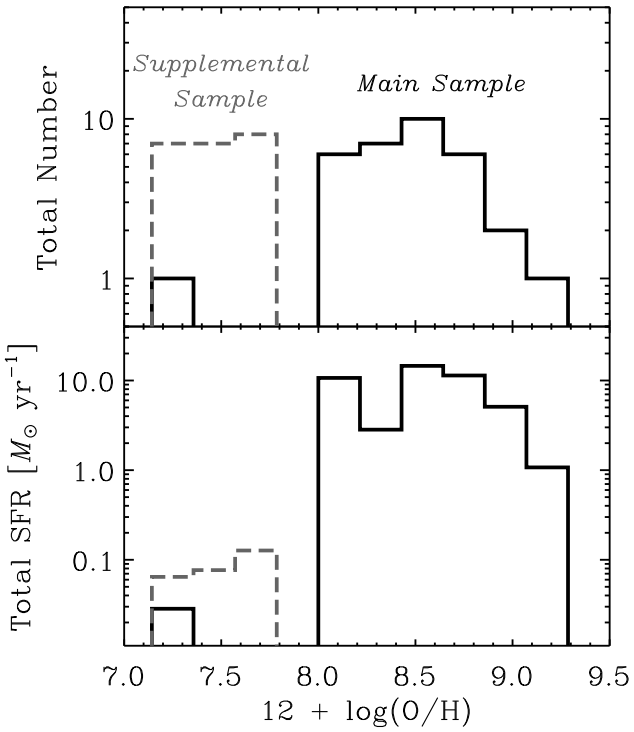

Figure 1. Sample distributions of metallicities ($12+\log(\mathrm{O/H})$) plotted in terms of total numbers of galaxies (*top panel*) and cumulative SFRs (*bottom panel*) per metallicity bin. Our main sample is shown as *solid black histograms* and our supplemental sample of 22 $12+\log(\mathrm{O/H}) < 8$ objects from Prestwich et al. (2013) is shown as *dashed gray histograms*. The cumulative SFR is a proxy for the number of HMXBs that are expected to be present within the galaxy sample. The supplemental sample has a low collective SFR and generally shallow *Chandra* observations. Although it helps to extend the metallicity range into the $12+\log(\mathrm{O/H}) < 8$ regime, the supplemental sample provides only weak constraints on the HMXB XLF.

The PP04 strong-line calibrations were empirically calibrated using direct-method measurements, and the two methods are consistent for $12+\log(\mathrm{O/H}) \approx$ 8.09–8.5. The direct method is generally considered to be robust for relatively low metallicities ($12+\log(\mathrm{O/H}) \lesssim 8.5$; e.g., Stasińska 2005). To bring the metallicities for our full galaxy sample into calibration alignment, we converted all 23 galaxies with KK04 estimates to the PP04 calibration using the methods described in

[1] Throughout this paper we quote metallicities in terms of gas-phase oxygen abundances, $12+\log(\mathrm{O/H})$, and take the solar value to be 8.69 (Allende Prieto et al. 2001). When comparing with theoretical models that specify metallicities explicitly, we assume the conversion $\log(Z/Z_\odot) = \log(\mathrm{O/H}) - \log(\mathrm{O/H})_\odot = \log(\mathrm{O/H}) - 3.31$.

Table 1. HMXB-Dominant Galaxy Sample and Properties

				Size Parameters								
Galaxy	Central Position		D	a	b	PA	$\log M_\star$	SFR	$12+\log(O/H)$	t_{exp}	$\log L_{50}$	
Name	α_{J2000}	δ_{J2000}	(Mpc)	(arcmin)		(deg)	($M_\odot$)	($M_\odot$ yr^{-1})	(dex)	(ks)	(erg s^{-1})	N_X
(1)	(2)	(3)	(4)	(5)	(6)	(7)	(8)	(9)	(10)	(11)	(12)	(13)
Main Sample												
NGC0024.....	00 09 56.5	–24 57 47.3	7.30±2.30	1.38	0.39	43.5	8.64	0.04	8.59±0.18	43	36.8	8
NGC0337.....	00 59 50.1	–07 34 40.7	22.40±2.30	0.87	0.49	157.5	9.32	1.09	8.44±0.07	9	38.5	6
NGC0628 (M74)....	01 36 41.8	+15 47 00.5	7.30±1.40	2.10	1.80	87.5	9.48	0.33	8.54±0.15	268	36.4	43
NGC0925.....	02 27 16.9	+33 34 44.0	9.12±0.17	1.87	0.82	105.0	9.03	0.18	8.38±0.15	12	37.5	7
NGC1482.....	03 54 38.9	–20 30 08.8	23.20±2.30	1.42	0.82	105.5	10.43	4.80	8.52±0.16	28	38.3	7
Supplemental Sample												
6dFJ0405204-364859	04 05 20.3	–36 49 01.0	11.00±0.00	0.23	0.19	16.5	...	0.006	7.34±0.09	5	38.0	0
HS0822+3542.....	08 25 55.5	+35 32 32.0	12.70±0.00	0.10	0.05	141.4	...	0.003	7.44±0.06	5	38.2	0
HS1442+4250.....	14 44 12.8	+42 37 44.0	10.50±0.00	0.44	0.10	63.2	...	0.011	7.64±0.02	5	37.8	0
IZw18.....	09 34 02.0	+55 14 28.0	17.10±0.00	0.13	0.09	145.0	...	0.045	7.18±0.03	40	37.6	1
J081239.52+483645.3	08 12 39.5	+48 36 45.0	9.04±0.00	0.21	0.11	73.7	...	0.001	7.28±0.06	4	37.9	0

NOTE—The full version of this table contains 15 columns of information for all 33 and 22 galaxies from our main and supplemental samples, respectively (see Section 2). An abbreviated version of the table is displayed here to illustrate its form and content. Col.(1): Adopted galaxy designation with Messier designation, if applicable. Col.(2) and (3): Right ascension and declination of the galactic center. Col.(4): Adopted distance and 1σ uncertainties in units of Mpc. Col.(5)–(7): Isophotal ellipse parameters, including, respectively, semi-major axis, a, semi-minor axis, b, and position angle east from north, PA. The majority of the main-sample galaxies have size parameters based on 2MASS K_s-band data from Jarrett et al. (2003). In these cases, the K_s-band 20 mag arcsec^{-2} ellipses were used to avoid large contamination from background sources; however, for galaxies with K_s-band 20 mag arcsec^{-2} semi-major axes $a < 1$ arcmin, we chose to adopt the "total' K_s-band ellipses. For the main-sample galaxies DDO68, NGC 4861, and IC2574, and all galaxies in the supplemental sample, we adopted the positions and D_{25} sizes using the HyperLeda database (http://leda.univ-lyon1.fr/). Col.(8): Logarithm of the galactic stellar mass, $M_\star$, within the regions defined. Col.(9): Star-formation rate within the defined regions. Col.(10): Adopted estimate of the average oxygen abundances, $12+\log(O/H)$; see Col.(15) for references. For consistency with other studies of XRB scaling relations that include metallicity, we have converted all abundances to the Pettini & Pagel (2004; PP04) calibration following the prescriptions in Kewley & Ellison (2008). Col.(11): Cumulative *Chandra* exposure time in ks. Col.(12): Logarithm of the 0.5–8 keV luminosity corresponding to 50% completeness across the galaxy. Col.(13): Number of X-ray detected sources within the galactic footprints defined by Col.(2)–(3) and (5)–(7). Col.(14) and (15): References to the adopted distances and $12+\log(O/H)$, respectively.

References.– 1=Moustakas et al. (2010); 2=Engelbracht et al. (2008); 3=Sacchi et al. (2016); 4=McQuinn et al. (2016); 5=Tully et al. (2013); 6=Freedman et al. (2001); 7=Nataf et al. (2015); 8=Skillman et al. (2013); 9=Bresolin et al. (2009); 10=Monreal-Ibero et al. (2012); 11=Hu et al. (2018); 12=Prestwich et al. (2013); 13=Guseva et al. (2007); 14=Izotov et al. (2006); 15=Izotov & Thuan (2007); 16=Izotov et al. (2007); 17=Izotov et al. (2012); 18=Papaderos et al. (2008); 19=Pustilnik et al. (2003); 20=van Zee (2000)

Kewley & Ellison (2008). In Col.(10) of Table 1, we provide the adopted metallicity values for our sample galaxies.

Following the procedures in L19, we generated SFR and $M_\star$ maps for main-sample galaxies using the scaling relations from Hao et al. (2011) and Zibetti et al. (2009), respectively. Values of the SFR and $M_\star$ quoted for each galaxy were extracted from the maps using the regions defined in Table 1, with NGC 0628, NGC 5194, and NGC 7552 having central regions removed due to potential AGN or confusion. The removal regions were located at the central positions of the galaxies and were circular in shape with radii of r_{remove} = 3 arcsec for NGC 0628 and NGC 5194, and r_{remove} = 15 arcsec for NGC 7552.

For the supplemental sample galaxies, we utilized the extinction-corrected values of L_{FUV}^{corr} from Prestwich et al. (2013), combined with the relation of Hao et al. (2011), to estimate SFR values. As per previous investigations of this sample (Prestwich et al. 2013; Brorby et al. 2014, 2016; Douna et al. 2015), we do not provide stellar mass estimates for these galaxies. These galaxies were originally selected as blue and actively star forming, and are expected to have high sSFRs and contain negligible contributions from LMXBs.

As discussed in Section 1, for consistency with other work, the values of SFR and $M_\star$ above assume conversion factors using solar abundances and do not incorporate variations due to metallicity. Applying such a variation would have its largest impact on the young massive star population, in which low-metallicity stars are expected to be hotter and produce more UV emission per unit SFR compared to the solar abundance case (e.g., Bicker & Fritze-v. Alvensleben 2005). We have calculated, using PÉGASE models (Fioc & Rocca-Volmerange 1997) for constant SFHs over 100 Myr, that the SFR/L_{FUV} conversion factors would be ≈0.8 and ≈1.2 times the solar-value factor at $12+\log(O/H)$ = 7 and 9.2, respectively. Given that past results, as well as the results presented below, show a decline in L_X/SFR with increasing metallicity, including the metallicity dependence in the SFR calculations

would act to further promote such a trend at a maximium level of ≈0.18 dex across the full metallicity range.

In Table 1, we list the physical properties of galaxies in our main and supplemental samples. Our main sample contains galaxies with SFR = 0.02–9.0 $M_\odot$ yr^{-1} ($\langle$SFR$\rangle$ = 1.4 $M_\odot$ yr^{-1}) and log$M_\star/M_\odot$ = 7.3–10.4 (log$\langle M_\star/M_\odot\rangle$ = 9.7). Our supplemental sample has a range of SFR = 0.0007–0.045 $M_\odot$ yr^{-1} ($\langle$SFR$\rangle$ = 0.012 $M_\odot$ yr^{-1}). Figure 1 shows binned distributions of oxygen abundances for our main and supplemental samples in terms of numbers of galaxies and cumulative SFR in each bin. Given the HMXB XLF scaling with SFR, the SFR of a given bin can be considered a proxy for the total number of HMXBs present in the samples. It is clear that the extremely metal-poor galaxy subsample is expected to harbor fewer HMXBs than the main sample, given its low cumulative SFR.

In addition to the relatively low SFRs compared to the main sample, the supplemental sample has available only relatively shallow *Chandra* exposures (see Section 3 for a detailed discussion of the *Chandra* data). The supplemental sample mean *Chandra* exposure is ≈10 ks, compared with ≈150 ks for the main sample. The combination of these two factors (relatively low SFR and shallow *Chandra* data) lead to the supplemental sample containing ≈200 times fewer X-ray detected point sources within the galaxy footprints compared to the main sample. In fact, the majority of the supplemental sample galaxies (17 out of 22) contain no detected point sources coincident with the galaxies, while all main sample galaxies have at least one detected source.

3. DATA ANALYSIS

We chose to incorporate all ACIS-S or ACIS-I *Chandra* imaging observations with aim-points less than 5 arcmin from the galactic centers (see Col.(3) and (4) in Table 1). This led to the selection of 137 and 22 ObsIDs for the 33 and 22 galaxies in our main and supplementary samples, respectively. The cumulative *Chandra* exposures spanned the range of 5–853 ks (see Col.(12) of Table 1).

Our *Chandra* data analysis procedure follows that presented in Section 3.2 of L19; we briefly describe our procedure here. For a given galaxy, we reprocessed all ObsIDs to the most recent calibrations, removed bad events from bad columns and pixels, and generated exposure maps. When more than one ObsID was available, we aligned all observations to the longest exposure, and co-added all observations for the purpose of identifying X-ray point sources. X-ray point sources were identified by running `wavdetect` on ObsID-merged images in the 0.5–2 keV, 2–7 keV, and 0.5–7 keV bands, and resulting point source properties were analyzed using `ACIS Extract` (`AE`; Broos et al. 2010, 2012). For each galaxy, `AE` first analyzes all ObsIDs separately and subsequently combines them to provide appropriate source photometry and spectra. `AE` then performs spectral fitting and provides flux measurements for all point sources, which are used for our X-ray point source catalogs.[2]

For each galaxy, we assessed point-source completeness (i.e., fraction of sources recovered by our procedure as a function of luminosity L) by running simulations where

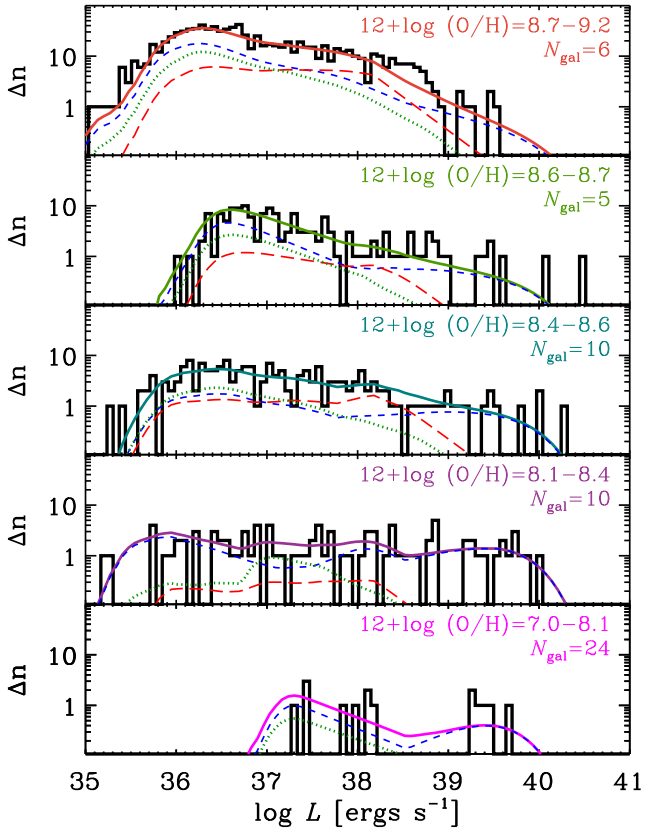

Figure 2. Observed distributions of X-ray point-source luminosities for galaxy subsamples binned by 12 + log(O/H) (*black histograms*). The metallicity range and number of galaxies within the bin, N_{gal}, are annotated in each panel. The detailed shapes and X-ray luminosity ranges of the distributions are dependent on both the intrinsic distributions of the point-source populations as well as the completeness characteristics of the observations, which can vary substantially among galaxies. Our best-fit metallicity-dependent HMXB XLF model predictions are shown as *short-dashed blue curves*, with the model contributions from CXB sources and LMXBs shown as *dotted green* and *long-dashed red curves*, respectively. The CXB and LMXB model contributions for each galaxy vary with X-ray completeness and scale only with the galaxy sky coverage and stellar mass, respectively, and do not vary with metallicity (see Section 3 for details). The summed contributions of these model components constitute our total point-source models, which are shown in each panel as *solid curves of varying color*.

[2] Point-source catalogs are summarized in Appendix A and provided in the electronic version of the paper.

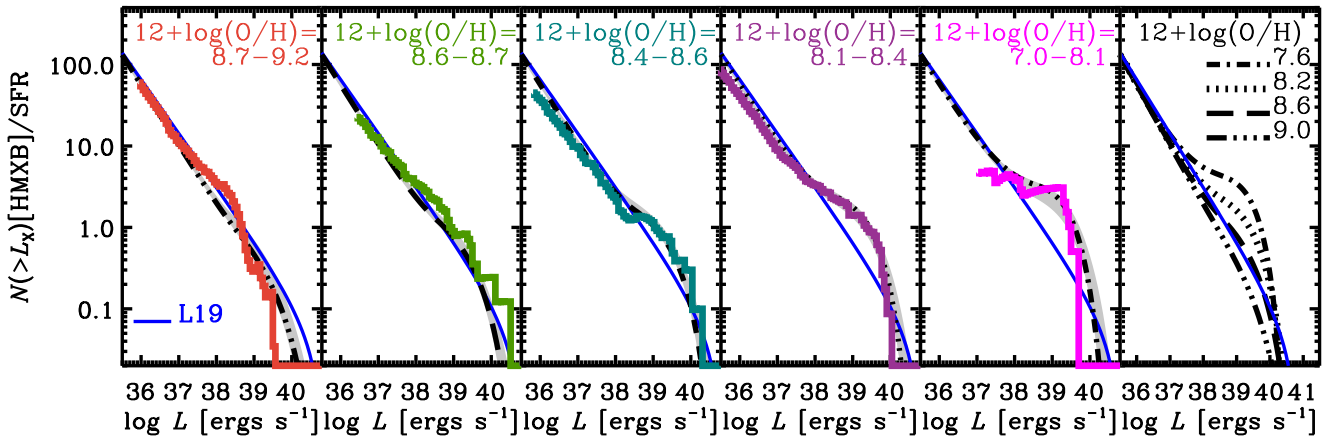

Figure 3. *First Five Panels*: SFR-normalized cumulative HMXB XLFs for the five metallicity bins explored in this study. Data have been plotted in various colors, following the colors in Figure 2, and are shown here with model CXB and LMXB contributions subtracted and completeness corrected. Thus, some regions in the cumulative plot appear to show small decreases in $N(>L)$ with decreasing L due to CXB contributions being non-negligible (e.g., in the low-metallicity regime). We limited the dispayed luminosity range to be above the lowest 50% completeness limit among the galaxies that make up each subsample. In each panel, our metallicity-dependent HMXB XLF model (*black curves*) is dispayed with 1σ uncertainty (*gray shaded region*), and the L19 best-fit HMXB model for local galaxies is shown in all panels as a blue solid line. *Final Panel*: Our best-fit metallicity-dependent HMXB XLF model at various metallicities (see annotations). The best-fit model and data reveal a flattening of the HMXB XLF at $L \gtrsim 10^{38}$ erg s^{-1} and overall elevation of the number of bright source per unit SFR with declining metallicity.

mock sources were added to images (using MARX point-spread functions generated by AE and custom software) and tested for recovery by re-running our procedure. These completeness curves are critical for correctly modeling the XLFs. The resulting 50% completeness limits span $\log L_{50}$(erg s^{-1}) = 35.9–38.5 and are listed in Col.(13) of Table 1. Given the variations in *Chandra* exposure, distance, and galaxy type, the number of X-ray point-sources detected in the galaxy footprints ranges from 0–363 (see Col.(14) in Table 1).

To build our metallicity-dependent HMXB XLF model, we first divided our combined main and supplemental galaxy samples into five bins of 12+log(O/H) that were chosen to have similar cumulative SFRs (except for the lowest metallicity bin). For each bin, we constructed an observed distribution of luminosities using all point-sources (including HMXBs, LMXBs, and background sources) collected for all galaxies in the bin. These distributions are presented as histograms for the five metallicity bins in Figure 2 (*black histograms*). Using our derived completeness functions, along with galactic sky area and $M_\star$ measurements, we estimated for each galaxy the expected contribution to the point-source luminosity distribution for unrelated background sources from the cosmic X-ray background (hereafter, CXB) and LMXBs, respectively. We utilized extragalactic number counts from Kim et al. (2007) to estimate the CXB component, and the $M_\star$-normalized LMXB relation from L19 to estimate LMXB contributions. For all cases, the CXB and LMXB model components (shown as green-dotted and red long-dashed curves in Figure 2) were comfortably below the observed X-ray point-source distributions, and indicate that our selection criteria result in a dominance of HMXB populations.

In Figure 3, we show the CXB-and-LMXB subtracted and completeness-corrected cumulative XLF for each of the metallicity ranges, normalized by the cumulative SFR in each bin. For comparison, the average HMXB XLF model fit from L19, which consists of a single-slope power-law with a cut-off luminosity, is displayed in each panel (*thin blue curves*). We stress that this representation of the data was not used when fitting for the metallicity-dependent HMXB XLF (see below), due to its cumulative form, subtraction of model components (i.e., CXB and LMXBs), and large corrections for completeness at the low-L ends of the distributions. However, this representation provides guidance on the overall form of the metallicity dependence to the shape and normalization of the HMXB XLF.

The data in Figure 3 show clear trends with metallicity, which can be gleaned from comparisons with the L19 HMXB XLF curve (*blue solid curve*). HXMB XLFs at all metallicities show similar steep power-law like slopes and SFR normalizations at $L \lesssim$ (3–10) $\times 10^{37}$ erg s^{-1}. However, at $L \gtrsim 10^{38}$ erg s^{-1} the distribution flattens and extends to increasingly higher luminosities with declining metallicity. For example, we find that the number of ULXs (i.e., $L > 10^{39}$ erg s^{-1}) per SFR increases from $\approx$0.5 $(M_\odot\ \mathrm{yr}^{-1})^{-1}$ to $\approx$2 $(M_\odot\ \mathrm{yr}^{-1})^{-1}$ from 12+log(O/H) $\approx$9 to 8 (see Section 5.1 for further discussion on ULXs).

The trends observed in Figure 3 indicate that the L_X–SFR–Z relations that have been examined in the literature (see Sec-

tion 1 and references therein) result from a complex variation in the bright-end of the HMXB XLF with metallicity, instead of a simple change in normalization, as has been proposed in previous investigations (e.g., Brorby et al. 2014; Basu-Zych et al. 2016; Ponnada et al. 2020). Motivated by the observed metallicity-dependent HMXB XLF behavior in Figure 3, we chose to model the data using the following functional form:

$$\frac{dN_{\rm HMXB}}{dL} = {\rm SFR}\, A_{\rm HMXB}\, \exp[-L/L_{\rm c}(Z)] \times \begin{cases} L^{-\gamma_1} & (L < L_b) \\ L_b^{\gamma_2(Z)-\gamma_1} L^{-\gamma_2(Z)}, & (L > L_b) \end{cases} \quad (1)$$

where

$$\gamma_2(Z) = \gamma_{2,\odot} + \frac{d\gamma_2}{d\log Z}[12+\log({\rm O/H})-8.69], \quad (2)$$

and

$$\log L_{\rm c}(Z) = \log L_{c,\odot} + \frac{d\log L_{\rm c}}{d\log Z}[12+\log({\rm O/H})-8.69]. \quad (3)$$

The above model contains seven free parameters, including both *metallicity-invariant parameters* like the overall normalization per SFR, $A_{\rm HMXB}$, the broken power-law component faint-end slope, γ_1, and break luminosity, L_b, as well as the *metallicity-dependent* bright-end power-law slope, $\gamma_2(Z)$, and exponential cut-off luminosity, $L_{\rm c}(Z)$. The latter, metallicity-dependent quantities each include solar metallicity reference values ($\gamma_{2,\odot}$ and $\log L_{c,\odot}$) and their first derivative with respect to the logarithm of the metallicity ($d\gamma_2/d\log Z$ and $d\log L_c/d\log Z$).

To fit the parameterization specified by Equations (1)–(3), we made use of the MCMC approach described in Sections 4.1 and 4.3 of L19. For a given galaxy, the X-ray point-source luminosity distribution (equivalent to Figure 2 but for each galaxy individually) was modeled as:

$$M(L) = \xi(L)\Delta\log L\left[\frac{dN_{\rm HMXB}}{d\log L} + \frac{dN_{\rm LMXB}}{d\log L} + {\rm CXB}(L)\right], \quad (4)$$

where the $\xi(L)$ is the luminosity-dependent completeness function for the galaxy, and $dN_{\rm LMXB}/d\log L$ and CXB(L) are the LMXB XLF and differential number counts, respectively. The $dN_{\rm LMXB}/d\log L$ and CXB model components are uniquely specified for a galaxy, given its stellar mass and sky area, respectively. Although we expect the LMXB component to have some metallicity dependence, we note that (1) the metallicity range associated with the old stellar populations that harbor the LMXBs is likely to be smaller than the gas-phase metallicity values used here since the LMXBs would have formed at earlier epochs of cosmic history; (2) the metallicity dependence of LMXB formation is predicted to be weaker than that of the HMXB population (see, e.g., Figure 2 of Fragos et al. 2013a); and (3) the LMXB component is expected to be negligible for the majority of our galaxies with $12+\log({\rm O/H}) \lesssim 8.5$, even if some plausible metallicity dependence is applied.

Table 2. Metallicity-Dependent HMXB XLF Model

PARAMETER NAME	UNITS	VALUE
$A_{\rm HMXB}$	$(M_\odot\ {\rm yr}^{-1})^{-1}$	$1.29^{+0.18}_{-0.19}$
γ_1		$1.74^{+0.04}_{-0.04}$
$\log L_b$	log (erg s^{-1})	$38.54^{+0.12}_{-0.30}$
$\gamma_{2,\odot}$		$1.16^{+0.24}_{-0.10}$
$\log L_{c,\odot}$	log (erg s^{-1})	$39.98^{+0.34}_{-0.14}$
$\frac{d\gamma_2}{d\log Z}$	dex^{-1}	$1.34^{+0.23}_{-0.79}$
$\frac{d\log L_c}{d\log Z}$	dex dex^{-1}	$0.60^{+0.17}_{-0.49}$

Goodness of Fit Evaluation

SAMPLE	C	$C_{\rm exp}$	$C_{\rm var}$	$P_{\rm null}$
Metallicity-Averaged (All Bins)	**398**	**360**	**581**	**0.108**
12+log(O/H)= 8.70–9.20	94	79	139	0.218
12+log(O/H)= 8.55–8.70	75	68	109	0.495
12+log(O/H)= 8.38–8.55	69	79	140	0.429
12+log(O/H)= 8.10–8.38	109	87	143	0.060
12+log(O/H)= 7.00–8.10	51	47	50	0.574
Universal (All Galaxies)	**1247**	**1040**	**1867**	**<0.001**
Sources with $P_{\rm null} < 0.05$				
NGC0024	24	11	29	0.019
NGC0337	26	11	25	0.002
NGC0925	31	12	28	<0.001
NGC5408	30	11	32	<0.001
NGC5474	44	11	28	<0.001
RC2A1116+51	8	1	9	0.024
SBS0940+544	9	1	8	0.004

In our fitting procedure, an MCMC model was quantitatively compared with the observed distributions of X-ray point-source luminosities, $N(L)$, and evaluated on a global basis using the C-statistic (Cash 1979):

$$C = 2\sum_{i=1}^{n_{\rm gal}}\left(\sum_{j=1}^{n_{\rm X}} M_{i,j} - N_{i,j} + N_{i,j}\ln(N_{i,j}/M_{i,j})\right), \quad (5)$$

where $n_{\rm gal}$ = 55 galaxies in our sample (ith index), and $n_{\rm X}$ = 100 X-ray luminosity bins (jth index) spanning $\log L$(erg s^{-1}) = 35–41.7. We note that the majority of our galaxies do not have non-zero completeness across all 100 X-ray luminosity bins, and bins with zero completeness do not contribute to C.

4. RESULTS

In Table 2, we provide the resulting MCMC median and 16–84% confidence range for each parameter in our model, which is specified in Equations (1)–(3). We adopt the "best

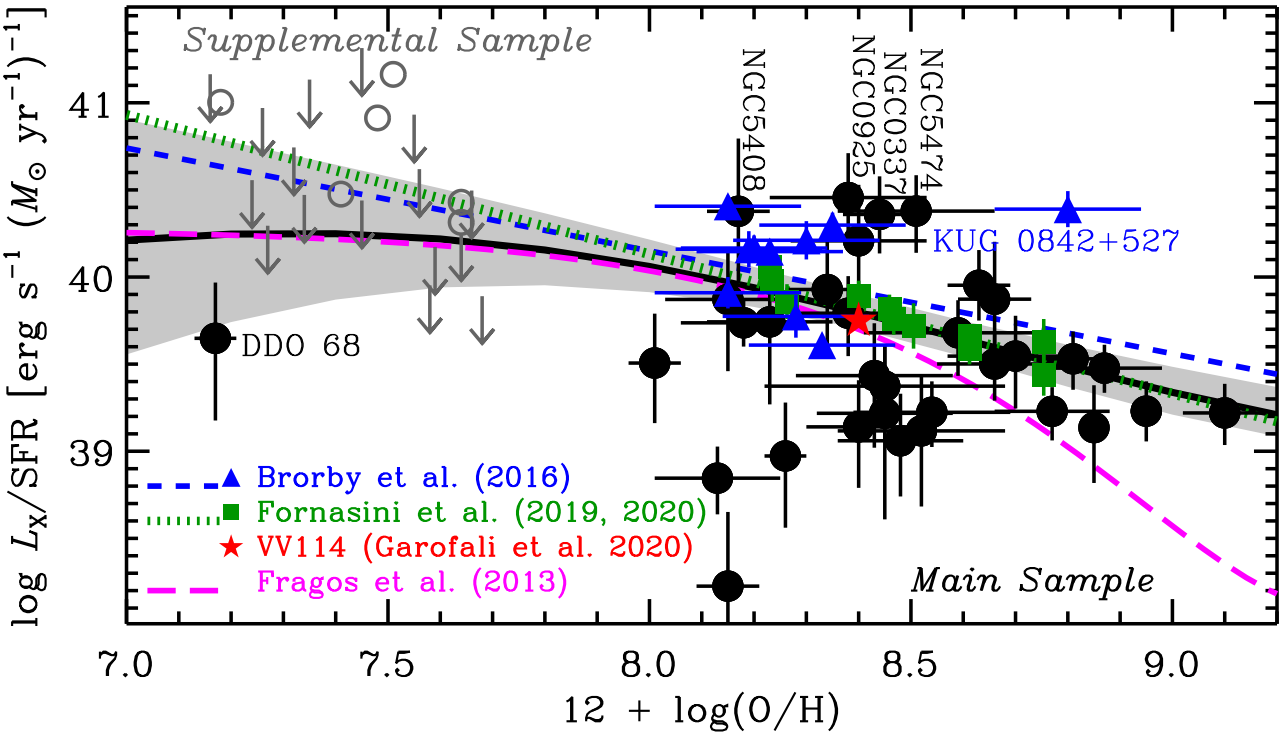

Figure 4. Galaxy-integrated HMXB population L_X/SFR versus metallicity (12+log(O/H)) for the galaxies in our main (*black filled circles*) and supplemental (*gray open circles and 84% confidence upper limits*) samples and our best-fit metallicity-dependent XLF model (*black solid curve with 1σ model uncertainty range*). Uncertainty related to stochasticity is not included in this uncertainty range; however, its impact is discussed and quantified in Section 5.1. L_X values for main-sample galaxies represent the estimated HMXB X-ray luminosities after correcting for model contributions from LMXB and CXB sources. For the supplemental galaxies, L_X values and upper limits are taken from Douna et al. (2015). For comparison, we overlay the locations of 10 Lyman break analogs from Brorby et al. (2016; *blue triangles*), 12 stacked samples of $z \approx 0.1$–2.6 galaxies from Fornasini et al. (2019, 2020; *green squares*), and the high-SFR, low-metallicity galaxy VV 114 (Garofali et al. 2020; *red star*). The best-fit power-law models from Brorby et al. (2016) and Fornasini et al. (2020) are shown as *blue-dashed* and *green-dotted* curves, respectively, and the Fragos et al. (2013b) XRB population synthesis model trend is shown as a *magenta long-dashed* curve.

model" as the model in our MCMC run that produced the minimum value of C in Eqn. (5). Our best model XRB source count distributions and SFR-normalized cumulative HMXB XLFs are shown for the five 12+log(O/H) bins in Figures 2 and 3, respectively.

Our best-fit model recovers the main observed features of the metallicity-dependent HMXB XLF discussed in Section 3, including the transition from a nearly single power-law slope at high metallicity to a broken power-law with a relatively flat extension at $L \approx$ (1–50) $\times 10^{38}$ erg s^{-1} at low metallicity. At solar metallicity, our HMXB XLF slopes straddle the best-fit single power-law values presented by Mineo et al. (2012a) and L19 and are consistent with values presented in studies of HMXB XLFs that are based on direct-counterpart classifications of X-ray sources (e.g., Tüllmann et al. 2011 and Williams et al. 2015 for M33 and Chandar et al. 2020 for M101).

We evaluated the goodness of fit of our model in both a "metallicity-averaged" and more stringent "universal" regime. In the metallicity-averaged regime, we assessed whether our model provided a good characterization of the average metallicity-dependent HMXB XLF using the data and model as represented by the five metallicity bins presented in Figure 2. We computed the C-statistic following Equation (5), replacing $n_{\rm gal}$ with $n_{\rm metal} = 5$ metallicity bins. We then used the methods of Kaastra (2017) to calculate the expected C-statistic, $C_{\rm exp}$, and its variance, $C_{\rm var}$, based on Poisson statistics, and evaluated the null-hypothesis probability, $P_{\rm null}$, following:

$$P_{\rm null} = 1 - {\rm erf}\left(\sqrt{\frac{(C - C_{\rm exp})^2}{2\,C_{\rm var}}}\right). \quad (6)$$

We found that in the metallicity-averaged sense, the data are statistically consistent with being drawn from our model, with $P_{\rm null} = 0.108$ overall, and $P_{\rm null} = 0.060$–0.574 for the five

bins (see Table 2). For comparison, the L19 HMXB XLF model (with no metallicity dependence) is ruled out, with $P_{\rm null} < 0.0001$ overall for the same data. However, the L19 model is acceptable only for the $12+\log({\rm O/H}) = 8.6$–8.8 and 8.4–8.6 bins ($P_{\rm null} = 0.857$ and 0.703, respectively), which is somewhat expected given that the majority of the L19 galaxies have metallicities in these ranges. The failure of the L19 model for the highest metallicity and two lowest metallicity bins further illustrates how our model is an improvement in the HMXB XLF characterization.

For the universal regime, we evaluated the null hypothesis probability using the C-statistic generated by Equation (5) for all 55 galaxies from the combined main and supplemental samples. This approach was used to determine our best-fit parameters in Section 3 and requires that all galaxies are reasonably well characterized by our model, since a small number of strong outliers can have a non-negligible influence on the total value of $P_{\rm null}$. Under this more strict evaluation, we found that our model was ruled out with $P_{\rm null} < 0.001$ overall. Thus, while our model provides a good characterization of how the "average" HMXB XLF varies with metallicity, it fails to provide a "universal" model of the HMXB XLF for all galaxies in our sample.

The failure of our model in the universal regime can be tied primarily to three of the 55 galaxies, NGC 925, NGC 5408, and NGC 5474, all of which are main-sample sources with $P_{\rm null} < 0.001$ and are deemed to be significant outliers. All four galaxies are observed to have excesses of $\approx$2–5 times the numbers of X-ray point sources compared to those predicted by our model without any clear trends with point-source luminosity (across $\log L({\rm erg\ s^{-1}}) = 37$–$39$). In addition to these significant outliers, there are an additional four galaxies that have some tension with our model at the $P_{\rm null} < 0.05$ level; we list these galaxies in Table 2. With the exception of NGC 1569, these galaxies also appear to have excesses of X-ray point-sources compared to the model. We expect that unmodeled physical variations in SFH, as well as gradients in the metallicities within the galaxies themselves, are plausible causes for the deviations from the model in the outlier population; we discuss these possibilities in more detail in Section 5.3. Despite its non-universality, our model provides a step forward in characterizing the metallicity dependence of the HMXB XLF, and hereafter we make use of this model in our discussions.

Our resulting metallicity-dependent HMXB XLF can be integrated to obtain the average $\langle L_{\rm X}/{\rm SFR}\rangle$ versus $12+\log({\rm O/H})$, a trend that has been explicitly studied in the literature. In Figure 4, we show $L_{\rm X}/{\rm SFR}$ versus $12+\log({\rm O/H})$ for the individual galaxies that make up our main and supplemental samples. These values were obtained by first modeling the XLF of a given galaxy using an HMXB component that consisted of a simple power-law with high-luminosity cut-off plus fixed CXB and LMXB components (following the procedure discussed in Section 3). The value of $L_{\rm X}/{\rm SFR}$ for a given galaxy was calculated by integrating the best-fit HMXB XLF for that galaxy, and thus excludes contributions from CXB and LMXB components.

For comparison, we show $L_{\rm X}/{\rm SFR}$ versus $12+\log({\rm O/H})$ for (1) 10 Lyman break analogs (LBAs) presented by Brorby et al. (2016); (2) 12 metallicity-binned stacked samples of galaxies spanning the redshift range $z \approx 0.1$–2.6 from the *Chandra* Deep Field (Fornasini et al. 2019) and the *Chandra* COSMOS (Fornasini et al. 2020) surveys; and (3) the location of the $L_{\rm X}$(XRB)/SFR from the low metallicity ($12+\log({\rm O/H}) \approx 8.4$) relatively distant, but high-SFR galaxy VV 114 (SFR $\approx 38\ M_\odot\ {\rm yr^{-1}}$), which has been spectrally decomposed by Garofali et al. (2020) using *Chandra*, *XMM-Newton*, and *NuSTAR* constraints.

Using our metallicity-dependent XLF model, we calculated probabilty distribution functions $P(\langle L_{\rm X}/{\rm SFR}\rangle | 12+\log({\rm O/H}))$ across a grid of $12+\log({\rm O/H})$ using our MCMC chains. At each value of $12+\log({\rm O/H})$, we calculated the median $L_{\rm X}/{\rm SFR}$ and 16–84% range implied by our model and its parameter uncertainties, which we show in Figure 4 (*black curve* and *gray shaded region*). In Col.(5) of Table 3, we tabulate the median values and 16–84% ranges of $L_{\rm X}/{\rm SFR}$ from our model.

For comparison with past studies, in Figure 4 we overlay the best-fit power-law models of $L_{\rm X}/{\rm SFR}$ versus $12+\log({\rm O/H})$ from Brorby et al. (2016; *blue-dashed line*) and Fornasini et al. (2020; *green-dotted line*).[3] We further overlay the XRB population synthesis theoretical best model median curve from Fragos et al. (2013b; *magenta long-dashed curve*).

In the $12+\log({\rm O/H}) > 8$ regime, our metallicity-dependent HMXB XLF model exhibits a trend in excellent agreement to the data and relation reported by Fornasini et al. (2020), albeit with a somewhat divergent trend appearing below $12+\log({\rm O/H}) \approx 8.2$, where no data was reported by Fornasini et al. The Brorby et al. (2016) relation is notably shallower and predicts relatively higher values of $L_{\rm X}/{\rm SFR}$ in this regime, compared to those found in this study and the Fornasini et al. (2020) relation. It is possible that contributions from LMXBs or AGN, which were not explicitly considered, could explain the relative elevation of the Brorby et al. relation. For example, the significant outlier at

[3] We note that displayed values of $L_{\rm X}/{\rm SFR}$ for comparison studies have been corrected from their original form to our adopted IMF and X-ray bandpass. Specifically, Brorby et al. (2016) $L_{\rm X}/{\rm SFR}$ values and relations have been increased by 0.25 dex to account for their use of the Salpeter IMF, and the $L_{\rm X}/{\rm SFR}$ values and relation from Fornasini et al. (2019, 2020) have been increased by 0.18 dex to convert their quoted 2–10 keV luminosities to 0.5–8 keV (based on their adopted power-law SED with $N_{\rm H} = 10^{21}$ cm^2 and $\Gamma = 2$).

Table 3. Model-Integrated Relations with Metallicity and SFR

	Model Expectation				Median and 16–84% $\log L_{\rm HMXB}^{\rm MC}$/SFR				
$12+\log({\rm O/H})$	N_{39}/SFR	$N_{39.5}$/SFR	N_{40}/SFR	$\langle\log(L_{\rm X}/{\rm SFR})\rangle$	(SFR = 0.01)	(0.1)	(1)	(10)	(100)
(1)	(2)	(3)	(4)	(5)	(6)	(7)	(8)	(9)	(10)
7.0.....	$4.29^{+7.63}_{-3.07}$	$1.60^{+5.64}_{-1.45}$	<1.9036	$40.21^{+0.69}_{-0.66}$	$38.16^{+0.75}_{-0.56}$	$38.82^{+1.53}_{-0.50}$	$39.92^{+0.22}_{-0.31}$	$39.95^{+0.07}_{-0.08}$	39.96±0.02
7.2.....	$4.27^{+5.09}_{-2.53}$	$1.80^{+3.76}_{-1.42}$	<1.3784	$40.25^{+0.53}_{-0.50}$	$38.16^{+0.77}_{-0.56}$	$38.89^{+1.56}_{-0.56}$	$40.04^{+0.22}_{-0.30}$	$40.07^{+0.07}_{-0.08}$	40.07±0.02
7.4.....	$3.97^{+3.26}_{-1.90}$	$1.83^{+2.38}_{-1.17}$	$0.20^{+0.93}_{-0.19}$	$40.25^{+0.40}_{-0.38}$	$38.16^{+0.77}_{-0.56}$	$38.93^{+1.59}_{-0.59}$	$40.11^{+0.22}_{-0.31}$	$40.14^{+0.07}_{-0.08}$	40.14±0.02
7.6.....	$3.47^{+2.01}_{-1.33}$	$1.68^{+1.42}_{-0.85}$	$0.26^{+0.59}_{-0.21}$	$40.22^{+0.29}_{-0.28}$	$38.16^{+0.77}_{-0.56}$	$38.89^{+1.64}_{-0.56}$	$40.13^{+0.23}_{-0.33}$	40.16±0.08	$40.17^{+0.02}_{-0.03}$
7.8.....	$2.84^{+1.19}_{-0.88}$	$1.41^{+0.81}_{-0.55}$	$0.27^{+0.34}_{-0.18}$	$40.16^{+0.21}_{-0.20}$	$38.16^{+0.74}_{-0.56}$	$38.83^{+1.65}_{-0.52}$	$40.09^{+0.26}_{-0.38}$	$40.14^{+0.08}_{-0.09}$	40.14±0.03
8.0.....	$2.20^{+0.68}_{-0.54}$	$1.09^{+0.44}_{-0.33}$	$0.24^{+0.19}_{-0.12}$	40.06±0.15	$38.15^{+0.73}_{-0.55}$	$38.77^{+1.58}_{-0.46}$	$40.00^{+0.31}_{-0.46}$	$40.07^{+0.10}_{-0.11}$	40.07±0.03
8.2.....	$1.62^{+0.37}_{-0.31}$	$0.77^{+0.23}_{-0.18}$	$0.19^{+0.11}_{-0.08}$	$39.94^{+0.12}_{-0.11}$	$38.15^{+0.72}_{-0.55}$	$38.71^{+1.37}_{-0.42}$	$39.85^{+0.37}_{-0.59}$	$39.96^{+0.12}_{-0.13}$	39.97±0.04
8.4.....	$1.15^{+0.21}_{-0.18}$	$0.51^{+0.13}_{-0.10}$	$0.13^{+0.06}_{-0.05}$	$39.80^{+0.10}_{-0.09}$	$38.15^{+0.70}_{-0.55}$	$38.67^{+1.00}_{-0.39}$	$39.63^{+0.48}_{-0.67}$	$39.81^{+0.14}_{-0.16}$	39.83±0.05
8.6.....	$0.80^{+0.17}_{-0.15}$	$0.32^{+0.09}_{-0.08}$	$0.08^{+0.04}_{-0.03}$	$39.64^{+0.11}_{-0.10}$	$38.14^{+0.69}_{-0.55}$	$38.65^{+0.75}_{-0.37}$	$39.37^{+0.57}_{-0.55}$	$39.64^{+0.17}_{-0.19}$	39.67±0.06
8.8.....	$0.54^{+0.17}_{-0.13}$	$0.20^{+0.08}_{-0.06}$	$0.05^{+0.03}_{-0.02}$	$39.49^{+0.13}_{-0.12}$	$38.14^{+0.69}_{-0.54}$	$38.62^{+0.64}_{-0.35}$	$39.14^{+0.59}_{-0.39}$	39.46±0.20	39.50±0.07
9.0.....	$0.37^{+0.16}_{-0.11}$	$0.11^{+0.07}_{-0.05}$	$0.03^{+0.02}_{-0.01}$	$39.34^{+0.15}_{-0.13}$	$38.14^{+0.68}_{-0.55}$	$38.62^{+0.58}_{-0.35}$	$39.01^{+0.49}_{-0.30}$	$39.28^{+0.22}_{-0.19}$	39.33±0.07
9.2.....	$0.25^{+0.15}_{-0.09}$	$0.07^{+0.06}_{-0.03}$	<0.0181	$39.21^{+0.16}_{-0.12}$	$38.14^{+0.67}_{-0.55}$	$38.60^{+0.55}_{-0.35}$	$38.95^{+0.38}_{-0.26}$	$39.13^{+0.20}_{-0.15}$	$39.19^{+0.07}_{-0.06}$

Note.—The modeled integrated SFR-normalized number of sources, integrated luminosity, and statistical median, 16%, and 84% expected values of $\log L_{\rm X}$/SFR for various SFR values. The statistical medians and 16–84% confidence intervals were obtained using Monte Carlo simulations described in Section 5.1, in which X-ray populations were stochastically sampled from our best-fit model.

$12+\log({\rm O/H})$ = 8.8, KUG 0842+527, has been reported to be a radio galaxy and have a large stellar mass (see Svoboda et al. 2019). Also in this regime we find that the Fragos et al. (2013b) best model appears consistent with our model from $12+\log({\rm O/H})$ = 8–8.5, but quickly diverges to much lower predictions of $L_{\rm X}$/SFR at higher metallicities. The divergence at metallicities above solar is likely due to the stellar-wind prescription becoming more aggressive in terms of removing mass from binary systems, resulting in a larger fraction of binaries avoiding mass-transfer (and X-ray luminous) phases. Stellar-wind prescriptions in this regime are highly uncertain, due to a lack of observationally constrained mass-loss rates.

In the extreme metal-poor regime, the uncertainties on our model increase substantially due to weak constraints. However, the trajectory of $L_{\rm X}$/SFR with metallicity for our model appears to flatten, diverging from a simple power-law extrapolation from Brorby et al. and Fornasini et al. It is certainly the case that a power-law form will become unphysical at some low value of metallicity, since the predicted $L_{\rm X}$ diverges for the metal-free case. In fact, the Fragos et al. (2013b) model predicts that a turnover will occur in this regime, consistent with our best fit model. Improved constraints on the XLF in this regime, through deeper observations and observations of additional galaxies, are required to definitively characterize this effect.

5. DISCUSSION

5.1. *The $L_{\rm X}$-SFR-Z Relation and its Scatter*

As discussed in Section 1, the $L_{\rm X}$-SFR-Z relation is of particular importance to a variety of astrophysical investigations. Such investigations may require, e.g., assessments of the likelihoods that specific X-ray detected objects are XRBs versus AGN, or estimates of the X-ray radiation field during the epoch of heating at $z \gtrsim 10$, where HMXBs are thought to dominate. For such studies, clear predictions for the $L_{\rm X}$-SFR-Z relation and its statistical scatter are of great use. In the discussion that follows, we assume that the statistical scatter is dominated by sampling stochasticity. Additional scatter related to luminous transient and variable source populations (e.g., BeXRBs and supergiant fast X-ray transients; see, e.g., Reig 2011 and Martínez-Núñez et al. 2017) is expected to be present, as well. Thus far, such forms of scatter have not been extensively investigated; however, a study of variable source populations in NGC 300 finds that variability does not have a detectable impact on the derived XLF for the galaxy (see, e.g., Binder et al. 2017). Nonetheless, future studies that assess how variable and transient source populations affect XLF scatter in a variety of environments would help clarify this picture.

Our metallicity-dependent HMXB XLF framework can be used to quantify statistical properties of the $L_{\rm X}$-SFR-Z relation beyond the model uncertainties discussed in Section 4. As shown by Gilfanov et al. (2004), XLFs with relatively shallow power-law slopes ($\gamma < 2$), like those representative of the HMXB population, result in integrated $L_{\rm X}$/SFR values that are subject to non-negligible stochastic scatter due to partial sampling of the full-L range of the XLF. For in-

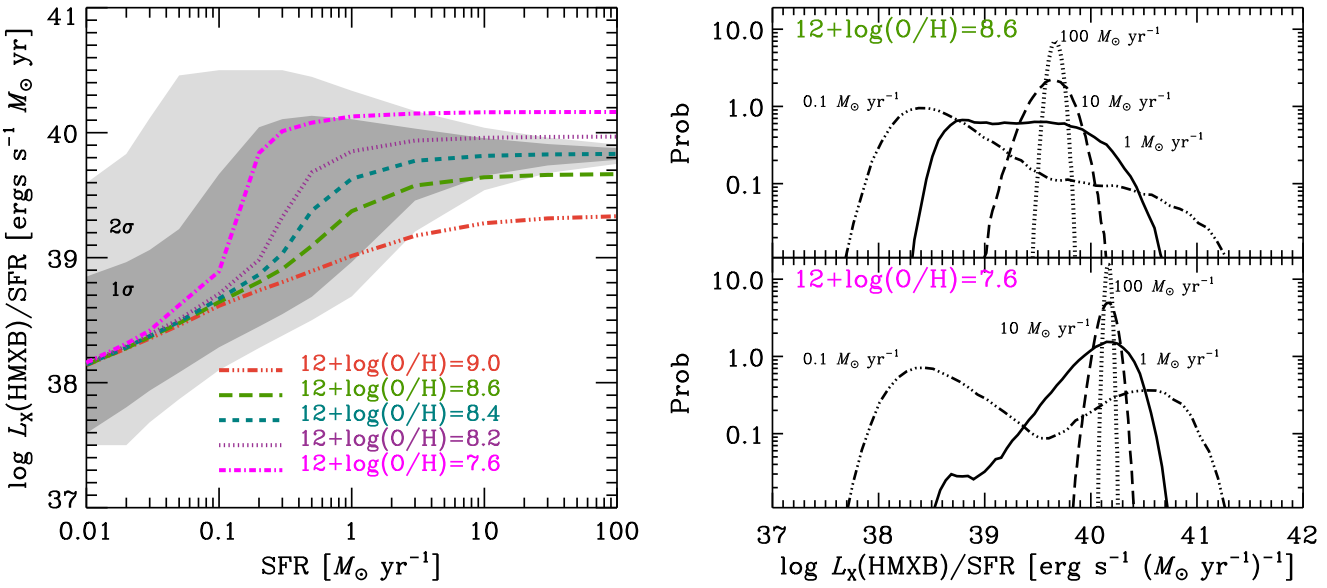

Figure 5. (*Left*) Our best-fit-model predictions for the median $\log L_X$/SFR versus SFR for five metallicity values (*continuous curves*; see annotation). The predicted stochastic scatter in the distribution of the $12+\log(O/H) = 8.4$ model is shown as dark and light gray shaded regions, representing 1σ and 2σ ranges, respectively. These regions only apply to the predicted scatter and do not include uncertainties in model fit parameters. The values corresponding to these curves, along with their scatter ranges, are tabulated in Table 3, Col. (6)–(10). (*Right*) Example probability distributions of $\log L_X$/SFR associated with the stochastic scatter predicted by our best metallicity-dependent HMXB XLF model for $12+\log(O/H) = 8.6$ (*top*) and 7.6 (*bottom*). Similar to the left panel, these distributions include only stochastic effects and do not contain the uncertainties associated with our model fit parameters. We display distributions at various SFR values (see annotations) and two metallicities to demonstrate the variety of distributions predicted by our model and the clear widening of the distributions going from high-to-low SFRs.

stance, the SFR-normalized cumulative XLF shown in the first panel of Figure 3 (i.e., for $12+\log(O/H)= 8.8$–9.2), suggests that a typical galaxy with SFR = 1 $M_\odot$ yr^{-1} would host a brightest source around $L_{max} \approx 3\times10^{38}$ erg s^{-1}, while a galaxy with SFR = 10 $M_\odot$ yr^{-1} would be expected to have $L_{max} \approx 10^{40}$ erg s^{-1}. For these cases, the typical (i.e., median) values of the L_X/SFR would be dominated by the brightest sources,

$$L_X/\mathrm{SFR} \approx \frac{1}{\mathrm{SFR}} \int_0^{L_{max}} \frac{dN}{dL} L\,dL \propto \frac{L_{max}^{2-\gamma}}{\mathrm{SFR}}, \qquad (7)$$

and would take on different values for the 1 $M_\odot$ yr^{-1} and 10 $M_\odot$ yr^{-1} galaxy populations. As a corollary, populations of galaxies at a fixed metallicity would be expected to have SFR-dependent statistical distributions and scatter of L_X/SFR, but with a SFR-independent mean value that follows the black curve in Figure 4. We note that the stochastic variations of L_X/SFR are not expected to influence our HMXB XLFs themselves, since we are using Poisson modeling of the differential XLF in narrow bins of L, including bins that extend well beyond the most luminous detected sources.

In addition to the SFR-dependent scatter, our HMXB XLF model shape is also metallicity dependent, which implies the statistical distributions of L_X/SFR are also metallicity dependent. To quantify the scatter-related SFR and metallicity dependent probability distribution functions of L_X/SFR, we employed Monte Carlo simulations following the procedures outlined in Section 5.3 of L19. Briefly, a given Monte Carlo trial uses a chosen pair of SFR and $12+\log(O/H)$ values to uniquely specify our model HMXB XLF (Eqns. 1–3), which provides a prediction for the total number of HMXBs, N^{MC}_{HMXB}, in the population and their L-dependent distribution. We then probabilistically sample from that distribution to assign luminosity values to the N^{MC}_{HMXB} simulated HMXBs, and sum the luminosities to generate L^{MC}_{HMXB}. This procedure is repeated 1,000 times to build up the distribution of L^{MC}_{HMXB} for the given SFR and $12+\log(O/H)$ pair. We note that this procedure provides stochastic distributions of L^{MC}_{HMXB} for the best-fit model solution and does not include parameter uncertainties. In Table 3 (Col. 6–10), we list the statistical properties inferred from our simulations, including the median and 16–84% limits on $\log L^{MC}_{HMXB}$/SFR for various SFR and $12+\log(O/H)$ pairs.

In the left panel of Figure 5, we show the median L^{MC}_{HMXB}/SFR versus SFR at five metallicity values (corresponding to values close to those used in Figs. 2 and 3). At high-SFR, all curves asymptote to the metallicity-dependent mean L_X/SFR values (i.e., Col.(5) in Table 3). However, at SFR $\lesssim$ 0.1, the curves for all metallicities converge to the similar values. This occurs when the expected brightest source in the distribution is below the break luminos-

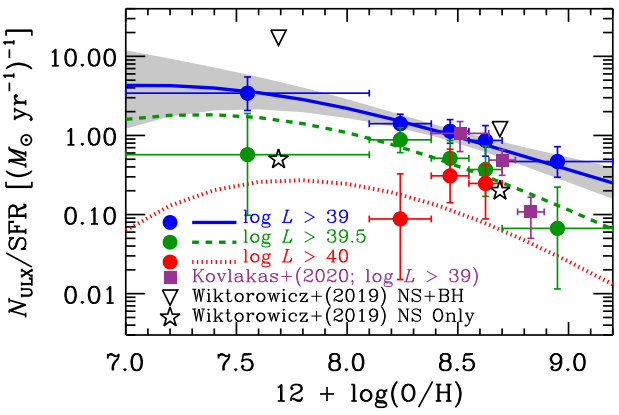

Figure 6. Number of ULXs per unit SFR as a function of metallicity for ULXs with $\log L > 39$, 39.5, and 40. Data points with full metallicity ranges and 1σ errors on $N_{\rm ULX}$/SFR represent the observed values for our sample, and continuous curves represent the predictions from our best-fit metallicity-dependent HMXB XLF model. The shaded region represents the 16–84% confidence range for our best-fit model prediction for sources with $\log L > 39$. These curves (as well as their uncertainties) are tabulated in Table 3. For comparison, the *lavender filled squares* show estimates for the frequency of $\log L(\mathrm{erg\ s^{-1}}) > 39$ sources in 40 late-type galaxies with $D < 40$ Mpc from Kovlakas et al. (2020). We also show the population synthesis predictions from Wiktorowicz et al. (2019) for the expected "observed" $N_{\rm ULX}$/SFR with $\log L > 39$ at 0.1 $Z_\odot$ and $Z_\odot$ for neutron star accretors (*open stars*) and neutron star plus black hole accretors (*open downward-pointing triangles*).

ity ($L_{\rm max} \ll L_b$), where our XLF model is metallicity independent (see the $L \leq L_b$ branch in Eqn. 1). For reference, we also display the 1σ and 2σ scatter regimes for the $12+\log(\mathrm{O/H}) = 8.4$ curve. Not surprisingly, the scatter decreases in size with increasing SFR, varying from $\approx$0.6 dex at SFR = 0.01 $M_\odot$ yr^{-1} to $\approx$0.05 dex at SFR = 100 $M_\odot$ yr^{-1}; at the high-SFR end, the scatter is expected to smaller than the current model uncertainty on $\langle L_{\rm X}/\mathrm{SFR}\rangle$ itself (see Col. 5 of Table 3).

In the right panel of Figure 5, we display the probability distributions of $L^{\rm MC}_{\rm HMXB}$/SFR at four SFR values for $12+\log(\mathrm{O/H}) = 7.6$ (bottom) and 8.6 (top). These distributions vary from high levels of skewness at low SFR (e.g., SFR = 0.1 and 1 $M_\odot$ yr^{-1}) and approach Gaussian-like distributions, centered around the mean, at SFR $\gtrsim$ 2–5 $M_\odot$ yr^{-1}. It is also apparent from the right-hand panels of Figure 5 that metallicity has a significant impact on the shapes of the distributions. For example, for SFR = 0.1 $M_\odot$ yr^{-1}, the median values of $L^{\rm MC}_{\rm HMXB}$/SFR are similar for both $12+\log(\mathrm{O/H}) = 7.6$ and 8.6, but their distributions are notably different at high $L^{\rm MC}_{\rm HMXB}$/SFR.

5.2. *Ultraluminous X-ray Source Populations*

As discussed above, our metallicity-dependent HMXB XLF analysis indicates that the $L_{\rm X}$-SFR-Z relation is driven primarily by a metallicity dependence in the $L > 10^{38}$ erg s^{-1} HMXB population. Of particular interest are ULXs (see, e.g., Kaaret et al. 2017b for a review), which are typically defined as off-nuclear X-ray sources with $L \gtrsim 10^{39}$ erg s^{-1}. Under isotropic emission assumptions (as used here), ULX luminosities can exceed the Eddington rates of 10–100 $M_\odot$ black holes. This fact has led to an assumption that ULXs primarily host black holes, with some potentially having "intermediate masses" of 10^2–$10^4 M_\odot$, well above black hole masses predicted by stellar evolution (e.g., Colbert & Mushotzky 1999).

Over the last decade, *XMM-Newton* and *NuSTAR* observations have revealed nearly ubiquitous high-energy turnovers at $E \gtrsim 3$ keV in ULX spectra, suggesting relatively cool Comptonization components and/or advection-dominated accretion disks, which are expected for stellar-mass accretors with super-Eddington mass-transfer rates and beamed emission (e.g., Gladstone et al. 2009; Sutton et al. 2013; Middleton & King 2016; Walton et al. 2018); however, some intermediate mass black hole candidates remain (e.g., HLX-1; Farrell et al. 2009). Recent discoveries of pulsations in several ULXs betray the neutron star nature of their accretors (Bachetti et al. 2014; Fürst et al. 2016; Israel et al. 2017; Brightman et al. 2018; Carpano et al. 2018; Earnshaw et al. 2018), sometimes revealing enormous beaming factors (e.g., M82 X-2 and NGC 5907 ULX1 have observed $L/L_{\rm Edd} \approx$ 100–500 assuming a 2 $M_\odot$ neutron star; Bachetti et al. 2014; Israel et al. 2017). Detailed binary evolution models suggest that such NS ULX binaries originate from intermediate X-ray binaries (e.g., Misra et al. 2020), which is in tension with parametric population synthesis models that predict $\approx M_\odot$ giant donor stars (e.g., Wiktorowicz et al. 2017).

Given their high luminosities and associations with star-forming galaxies (e.g., Swartz et al. 2011; Walton et al. 2011; Wang et al. 2016; Earnshaw et al. 2019; Kovlakas et al. 2020), ULXs are often assumed to be a subset of the HMXB population with young massive donor stars readily capable of driving large mass-transfer rates via Roche-lobe overflow (e.g., King et al. 2001). Studies aimed at isolating ULX counterparts have revealed direct associations with massive stars (see, e.g., Motch et al. 2014; Heida et al. 2019) or close spatial proximity to young luminous star clusters (e.g., Swartz et al. 2009; Poutanen et al. 2013; Egorov et al. 2017; Oskinova et al. 2019), providing direct evidence that many ULXs are indeed HMXBs. However, given the complexity of ULX accretion mechanisms, along with uncertainties in the distributions of accretor types and beaming factors in the observed population, theoretical models predict a large range of formation frequencies of ULXs within galaxies (i.e., number of ULXs per SFR or $M_\star$) that would be visible as ULXs

from Earth (e.g., Belczynski et al. 2004; Linden et al. 2010; King & Lasota 2016; Wiktorowicz et al. 2017, 2019; Kuranov et al. 2020). Going forward, these models would benefit from observational benchmarks such as those provided by our study.

In Figure 6, we show our constraints on the metallicity-dependent observed number of ULXs per SFR that have apparent luminosities (i.e., under the isotropic emission assumption) greater than 1, 3, and 10 $\times 10^{39}$ erg s^{-1}. Our XLF model constraints are overlaid as continuous curves, with the model uncertainty indicated as a shaded region for the 10^{39} erg s^{-1} case. These values are tabulated in Col. (2)–(4) in Table 3. For comparison, we show recent constraints from Kovlakas et al. (2020) on the ULX frequency as a function of $12+\log(\mathrm{O/H})$ for 40 late-type galaxies with $D < 40$ Mpc (*lavendar filled squares*). These estimates are based on a galaxy subsample that excluded elliptical/lenticular galaxies, galaxies with uncertain morphological classification in HyperLEDA ($e_t > 1.0$), objects without complete sky coverage, and sources where SFR and $M_\star$ were calculate in their HECATE catalog (see Kovlakas et al. 2020 for details). These estimates are in good agreement with our estimates, except at $12+\log(\mathrm{O/H}) \approx 8.8$, where the Kovlakas et al. (2020) ULX frequency is lower than our estimate by a factor of 2–5. Further investigations, beyond the scope of this paper, will be required to clarify the source of this discrepancy.

We further display, in Figure 6, the Wiktorowicz et al. (2019) population synthesis predictions of the ULX frequency for the case of a continuous SFH of 6 $M_\odot$ yr^{-1} over a period of 100 Myr (thus tracing HMXB ULXs) at 0.1 $Z_\odot$ and $Z_\odot$, which correspond to $12+\log(\mathrm{O/H})$ =7.69 and 8.69, respectively. These predictions are based on their `Startrack` XRB population synthesis models (Belczynski et al. 2002, 2008) and the mass-transfer-rate-dependent beaming prescriptions outlined in King et al. (2001) and King (2009). As such, the models account for the XRB populations that would appear as ULXs along a given line of sight, while tracking the intrinsic ULX population properties, including the accretor type. The predictions shown in Figure 6 correspond to the expected number of *observed* ULXs per SFR, after including the effects of beaming (i.e., as they would be observed externally). We show both the neutron star accretor and total (neutron star plus black hole) ULX predictions.

We find that the Wiktorowicz et al. (2019) predictions for neutron stars are somewhat lower than the total rates observed for all ULXs from this study. When including black holes, the theoretical ULX frequencies exceed the observations presented here. In the case of the 0.1 $Z_\odot$ population, the theoretical models are a factor of 5–10 times higher than those observed, suggesting that the black hole prescription itself overestimates the prevalence of these sources.

Since XRB population synthesis model predictions are highly variable depending on their assumptions (see, e.g., the case study by Tzanavaris et al. 2013), we are unable to make additional detailed physical conclusions about the nature of ULX accretors based on these results. For example, the population synthesis work by Kuranov et al. (2020) shows that highly magnetized neutron star accretors can produce ULX populations that are comparable to or larger than those predicted by Wiktorowicz et al. (2019), depending on the populations averaged magnetic moment and accretion disk structure. These models produce ULX luminosities through the accretion columns themselves and do not require strong beaming. These variations in predictions highlight the need for future population synthesis studies that use these empirical results as direct constraints on models.

5.3. *Towards a Universal Model for XRB XLFs*

In Section 4, we showed that our metallicity-dependent HMXB XLF model provides a statistically acceptable prescription for the average metallicity trends. Constraints on these trends can be improved with the combination of deeper and more numerous observations of the galaxies in the extreme metal-poor regime ($12+\log(\mathrm{O/H}) < 8$) that make up our supplemental sample (see, e.g., the constraints in this regime from Figures 2, 3, and 4). Building on the constraints in this regime will also be critical for clarifying the potential impact of HMXB radiation during the epoch of heating at $z \gtrsim 10$, when the majority of galaxies are expected to have abundances in this regime (see, e.g., Torrey et al. 2019).

Although our model is acceptable in a metallicity-averaged sense, it has been ruled out as universal (see Section 4). Given our large sample of 55 galaxies, we expect ≈3 galaxies to have $P_{\rm null} \leq 0.05$; however, none of the three galaxies listed in Table 2 with $P_{\rm null} \leq 0.001$ would be expected by statistical scatter alone.

Some *observational factors* that are not inherent to the HMXB populations themselves, such as enhanced absorption due to high disk inclinations or morphologically disturbed systems, could distort the observed XLFs and cause our model framework to be non-universal. However, we have eliminated the influence of such factors in our galaxies by our selection criteria, and the most egregious outliers in our sample (NGC 925, NGC 5408, and NGC 5474) are all found to have an excess of observed HMXBs over the model predictions suggesting some other factors *intrinsic* to the HMXB populations are at work.

As discussed in Section 1, in addition to metallicity, SFH variations of the $\lesssim 100$ Myr population can impact both the HMXB populations, as well as estimates on SFRs. Explicit theoretical predictions from Linden et al. (2010) and Wiktorowicz et al. (2017, 2019) suggest that the formation efficiencies of ULXs (e.g., number per unit stellar mass) can

vary by more than an order of magnitude within 10–100 Myr following a burst of star formation. Furthermore, less luminous HMXBs in the nearby Small Magellanic Clouds and M33, have also been shown to exhibit notable formation efficiency variations on these same timescales as the predominant XRB donor stars transition to lower masses with increasing age (e.g., Lehmer et al. 2017; Garofali et al. 2018; Antoniou et al. 2019).

Given the above, bursty SFHs like those found in low-mass, low-metallicity galaxies could easily result in variations in the HMXB XLF and the presence of a number of outlier galaxies in our sample. In future work, we plan to characterize the SFHs of a large number of local galaxies, including those in this work, and re-assess the combined influence of metallicity and SFH on the XLF. These steps will be crucial for ultimately developing a universal model for the XRB XLFs in galaxies.

6. SUMMARY

We have demonstrated that the SFR-normalized HMXB XLF depends on gas-phase metallicity, and we have provided a model detailing this dependence. Some of the key results from this study are included below.

1. We quantify and model the HMXB XLF across the luminosity range $\log L(\mathrm{erg\ s^{-1}}) \approx 36$–$41$ for 33 galaxies in the metallicity range of $12+\log(\mathrm{O/H}) = 7$–$9.2$. However, archival data for extremely metal-poor objects with $12+\log(\mathrm{O/H}) \lesssim 8$ contain only dwarf galaxies with relatively shallow data, limiting our HMXB XLF inferences in this metallicity range.

2. The impact of metallicity on the SFR-normalized HMXB XLF is most significant for HMXBs with $L \gtrsim 10^{38}$ erg s^{-1}. Below this limit, the XLF shape appears to follow a nearly universal power-law distribution, with slope $\gamma \approx 1.7$. Above this limit, the HMXB XLF goes from being power-law-like at nearly solar metallicities and then developing an increasingly flattened distribution with high-L cut-off as metallicity declines (see Figure 3).

3. We provide a new parameterization of the SFR-and-metallicity dependence of the HMXB XLF that provides a significant statistical improvement over constant SFR-dependent HMXB XLF models that have been widely used (see Sections 3 and 4 and comparison in Figure 3).

4. As a consequence of our results, we establish that the population-integrated $L_{\rm X}$–SFR–Z relations reported in the literature are driven by the metallicity-dependence of the $L \gtrsim 10^{38}$ erg s^{-1} population. For $12+\log(\mathrm{O/H}) \gtrsim 8.2$, our model predicts a similar $L_{\rm X}$–SFR–Z relation to Fornasini et al. (2020), but differs somewhat from that of Brorby et al. (2016) and the theoretical Fragos et al. (2013a) relations (see Figures 4 and 5, and Section 5.1). At $12+\log(\mathrm{O/H}) \lesssim 8$, our best-fit relation appears to flatten going to lower metallicity; however, our results are highly uncertain in this regime. Nonetheless, this behavior is similar to the theoretical predictions from Fragos et al. (2013a), but is different from the empirical extrapolations of power-law parameterizations presented in past studies (e.g., Brorby et al. 2016; Fornasini et al. 2020). Our model predictions for the $L_{\rm X}$–SFR–Z relation and its statistical properties are provided in Table 3.

5. Our HMXB XLF framework also allows for observational insight into the metallicity dependence of the ULX population. We quantify the metallicity and L dependence of the ULX population and compare with past population synthesis models from Wiktorowicz et al. (2019). Our ULX constraints are similar to the population synthesis predictions near solar metallicity; however, the observed ULX population is 5–10 times lower than predictions at $\approx 0.1\ Z_{\odot}$. Our constraints provide new benchmarks for future population synthesis studies and may aid in our understanding of the nature of these complex sources (see Section 5.2).

6. Finally, we show that a number of galaxies in our sample host HMXB populations that are significantly elevated compared to our model predictions. These galaxies are good candidates for harboring recent SFHs that deviate from the average young population within galaxies. Future studies that account for SFH will help to quantify the effect of SFH on the HXMB population (see Section 5.3).

We thank the anonymous referee for their helpful comments, which have improved the quality of this paper. We also thank Leslie Hunt for helpful discussions regarding galaxy sample selection. We gratefully acknowledge financial support from the NASA Astrophysics Data Analysis Program (ADAP) grant 80NSSC20K0444 (B.D.L., R.T.E.) and *Chandra* X-ray Center (CXC) grant GO7-18078X (B.D.L.). T.F. acknowledges support from the Swiss National Science Foundation Professorship grant (project number PP00P2 176868).

We made use of the NASA/IPAC Extragalactic Database (NED), which is operated by the Jet Propulsion Laboratory, California Institute of Technology, under contract with NASA. Our work includes observations made with the NASA *Galaxy Evolution Explorer* (*GALEX*). *GALEX* is operated for NASA by the California Institute of Technology

under NASA contract NAS5-98034. This publication makes use of data products from the Two Micron All Sky Survey (2MASS), which is a joint project of the University of Massachusetts and the Infrared Processing and Analysis Center/California Institute of Technology, funded by NASA and the National Science Foundation (NSF). This work is based on observations made with the *Spitzer Space Telescope*, obtained from the NASA/IPAC Infrared Science Archive, both of which are operated by the Jet Propulsion Laboratory, California Institute of Technology under a contract with NASA. We acknowledge the use of public data from the *Swift* data archive.

Facilities: *Chandra*, *Herschel*, *GALEX*, Sloan, *Spitzer*, *Swift*, 2MASS, DES, Pan-STARRS

Software: ACIS Extract (v2016sep22; Broos et al. 2010, 2012), MARX (v5.3.2; Davis et al. 2012), CIAO (v4.8; Fruscione et al. 2006), `xspec` (v12.9.1; Arnaud 1996), `Lightning` (Eufrasio et al. 2017), `PÉGASE` (Fioc & Rocca-Volmerange 1997)

REFERENCES

Aird, J., Coil, A. L., & Georgakakis, A. 2017, MNRAS, 465, 3390
Allende Prieto, C., Lambert, D. L., & Asplund, M. 2001, ApJL, 556, L63
Antoniou, V., Zezas, A., Drake, J. J., et al. 2019, ApJ, 887, 20
Arnaud, K. A. 1996, Astronomical Data Analysis Software and Systems V, 101, 17
Bachetti, M., Harrison, F. A., Walton, D. J., et al. 2014, Nature, 514, 202
Basu-Zych, A. R., Lehmer, B. D., Hornschemeier, A. E., et al. 2013a, ApJ, 762, 45
Basu-Zych, A. R., Lehmer, B. D., Hornschemeier, A. E., et al. 2013b, ApJ, 774, 152
Basu-Zych, A. R., Lehmer, B., Fragos, T., et al. 2016, ApJ, 818, 140
Belczynski, K., Kalogera, V., & Bulik, T. 2002, ApJ, 572, 407
Belczynski, K., Sadowski, A., & Rasio, F. A. 2004, ApJ, 611, 1068
Belczynski, K., Kalogera, V., Rasio, F. A., et al. 2008, ApJS, 174, 223
Bicker, J. & Fritze-v. Alvensleben, U. 2005, A&A, 443, L19
Binder, B., Gross, J., Williams, B. F., et al. 2017, ApJ, 834, 128
Birchall, K. L., Watson, M. G., & Aird, J. 2020, MNRAS, 492, 2268
Bluem, J., Kaaret, P., Prestwich, A., et al. 2019, MNRAS, 487, 4093
Bresolin, F., Ryan-Weber, E., Kennicutt, R. C., & Goddard, Q. 2009, ApJ, 695, 580
Brightman, M., Harrison, F. A., Fürst, F., et al. 2018, Nature Astronomy, 2, 312
Broos, P. S., Townsley, L. K., Feigelson, E. D., et al. 2010, ApJ, 714, 1582
Broos, P., Townsley, L., Getman, K., et al. 2012, AE: ACIS Extract, ascl:1203.001
Brorby, M., Kaaret, P., & Prestwich, A. 2014, MNRAS, 441, 2346
Brorby, M., Kaaret, P., Prestwich, A., & Mirabel, I. F. 2016, MNRAS, 457, 4081
Carpano, S., Haberl, F., Maitra, C., & Vasilopoulos, G. 2018, MNRAS, 476, L45
Cash, W. 1979, ApJ, 228, 939
Chandar, R., Johns, P., Mok, A., et al. 2020, ApJ, 890, 150
Colbert, E. J. M. & Mushotzky, R. F. 1999, ApJ, 519, 89
Colbert, E. J. M., Heckman, T. M., Ptak, A. F., Strickland, D. K., & Weaver, K. A. 2004, ApJ, 602, 231
Cseh, D., Grisé, F., Kaaret, P., et al. 2013, MNRAS, 435, 2896
Das, A., Mesinger, A., Pallottini, A., et al. 2017, MNRAS, 469, 1166
Dittenber, B., Oey, M. S., Hodges-Kluck, E., et al. 2020, ApJL, 890, L12
Douna, V. M., Pellizza, L. J., Mirabel, I. F., & Pedrosa, S. E. 2015, A&A, 579, A44
Dray, L. M. 2006, MNRAS, 370, 2079
Earnshaw, H. P., Roberts, T. P., & Sathyaprakash, R. 2018, MNRAS, 476, 4272
Earnshaw, H. P., Roberts, T. P., Middleton, M. J., et al. 2019, MNRAS, 483, 5554
Egorov, O. V., Lozinskaya, T. A., & Moiseev, A. V. 2017, MNRAS, 467, L1
Engelbracht, C. W., Rieke, G. H., Gordon, K. D., et al. 2008, ApJ, 678, 804
Eufrasio, R. T., Lehmer, B. D., Zezas, A., et al. 2017, ApJ, 851, 10
Farrell, S. A., Webb, N. A., Barret, D., et al. 2009, Nature, 460, 73
Fioc, M., & Rocca-Volmerange, B. 1997, A&A, 326, 950
Fornasini, F. M., Kriek, M., Sanders, R. L., et al. 2019, ApJ, 885, 65
Fornasini, F. M., Civano, F., & Suh, H. 2020, MNRAS, 495, 771
Fragos, T., Lehmer, B., Tremmel, M., et al. 2013a, ApJ, 764, 41
Fragos, T., Lehmer, B. D., Naoz, S., Zezas, A., & Basu-Zych, A. 2013b, ApJL, 776, L31
Freedman, W. L., Madore, B. F., Gibson, B. K., et al. 2001, ApJ, 553, 47
Fruscione, A., McDowell, J. C., Allen, G. E., et al. 2006, Proc. SPIE, 6270, 62701V
Fürst, F., Walton, D. J., Harrison, F. A., et al. 2016, ApJL, 831, L14
Garofali, K., Williams, B. F., Hillis, T., et al. 2018, MNRAS, 479, 3526

Garofali, K., Lehmer, B. D., Basu-Zych, A., et al. 2020, ApJ, 903, 79
Gilfanov, M. 2004, MNRAS, 349, 146
Gilfanov, M., Grimm, H.-J., & Sunyaev, R. 2004, MNRAS, 351, 1365
Gladstone, J. C., Roberts, T. P., & Done, C. 2009, MNRAS, 397, 1836
Greig, B., & Mesinger, A. 2018, MNRAS, 477, 3217
Grimm, H.-J., Gilfanov, M., & Sunyaev, R. 2002, A&A, 391, 923 P
Guseva, N. G., Izotov, Y. I., Papaderos, P., et al. 2007, A&A, 464, 885
Hao, C.-N., Kennicutt, R. C., Johnson, B. D., et al. 2011, ApJ, 741, 124
Heida, M., Lau, R. M., Davies, B., et al. 2019, ApJL, 883, L34
Heneka, C. & Mesinger, A. 2020, MNRAS, 496, 581
Hodges-Kluck, E., Gallo, E., Seth, A., et al. 2020, arXiv e-prints, arXiv:2006.16342
Hu, N., Wang, E., Lin, Z., et al. 2018, ApJ, 854, 68
Israel, G. L., Belfiore, A., Stella, L., et al. 2017, Science, 355, 817
Izotov, Y. I., Papaderos, P., Guseva, N. G., et al. 2006, A&A, 454, 137
Izotov, Y. I. & Thuan, T. X. 2007, ApJ, 665, 1115
Izotov, Y. I., Thuan, T. X., & Guseva, N. G. 2007, ApJ, 671, 1297
Izotov, Y. I., Thuan, T. X., & Guseva, N. G. 2012, A&A, 546, A122
Jarrett, T. H., Chester, T., Cutri, R., Schneider, S. E., & Huchra, J. P. 2003, AJ, 125, 525
Justham, S. & Schawinski, K. 2012, MNRAS, 423, 1641
Kaaret, P., Schmitt, J., & Gorski, M. 2011, ApJ, 741, 10
Kaaret, P., Brorby, M., Casella, L., et al. 2017a, MNRAS, 471, 4234
Kaaret, P., Feng, H., & Roberts, T. P. 2017b, ARA&A, 55, 303
Kaastra, J. S. 2017, A&A, 605, A51
Kennicutt, R. C., Jr., Armus, L., Bendo, G., et al. 2003, PASP, 115, 928
Kewley, L. J. & Ellison, S. L. 2008, ApJ, 681, 1183
Kim, M., Kim, D.-W., Wilkes, B. J., et al. 2007, ApJS, 169, 401
King, A. R., Davies, M. B., Ward, M. J., et al. 2001, ApJL, 552, L109
King, A. & Lasota, J.-P. 2016, MNRAS, 458, L10
Kobulnicky, H. A. & Kewley, L. J. 2004, ApJ, 617, 240 (KK04)
Koudmani, S., Henden, N. A., & Sijacki, D. 2020, arXiv:2007.10342
Kovlakas, K., Zezas, A., Andrews, J. J., et al. 2020, arXiv:2008.10572
Kouroumpatzakis, K., Zezas, A., Sell, P., et al. 2020, MNRAS, doi:10.1093/mnras/staa1063
Kroupa, P. 2001, MNRAS, 322, 231
Kuranov, A. K., Postnov, K. A., & Yungelson, L. R. 2020, arXiv:2010.03488
Latimer, C. J., Reines, A. E., Plotkin, R. M., et al. 2019, ApJ, 884, 78
Lehmer, B. D., Brandt, W. N., Alexander, D. M., et al. 2008, ApJ, 681, 1163
Lehmer, B. D., Alexander, D. M., Bauer, F. E., et al. 2010, ApJ, 724, 559
Lehmer, B. D., Basu-Zych, A. R., Mineo, S., et al. 2016, ApJ, 825, 7
Lehmer, B. D., Eufrasio, R. T., Markwardt, L., et al. 2017, ApJ, 851, 11
Lehmer, B. D., Eufrasio, R. T., Tzanavaris, P., et al. 2019, ApJS, 243, 3 (L19)
Lehmer, B. D., Ferrell, A. P., Doore, K., et al. 2020, ApJS, 248, 31
Linden, T., Kalogera, V., Sepinsky, J. F., et al. 2010, ApJ, 725, 1984
Liu, J., Orosz, J., & Bregman, J. N. 2012, ApJ, 745, 89
Liu, J.-F., Bregman, J. N., Bai, Y., et al. 2013, Nature, 503, 500
López, K. M., Jonker, P. G., Heida, M., et al. 2019, MNRAS, 489, 1249
Martínez-Núñez, S., Kretschmar, P., Bozzo, E., et al. 2017, SSRv, 212, 59
Madau, P., & Fragos, T. 2017, ApJ, 840, 39
Mapelli, M., Ripamonti, E., Zampieri, L., et al. 2010, MNRAS, 408, 234
McQuinn, K. B. W., Skillman, E. D., Dolphin, A. E., Berg, D., & Kennicutt, R. 2016, ApJ, 826, 21
Mezcua, M., Civano, F., Marchesi, S., et al. 2018, MNRAS, 478, 2576
Middleton, M. J. & King, A. 2016, MNRAS, 462, L71
Mineo, S., Gilfanov, M., & Sunyaev, R. 2012a, MNRAS, 426, 1870
Mineo, S., Gilfanov, M., & Sunyaev, R. 2012b, MNRAS, 426, 1870
Misra, D., Fragos, T., Tauris, T., et al. 2020, arXiv:2004.01205
Mesinger, A., Ferrara, A., & Spiegel, D. S. 2013, MNRAS, 431, 621
Mirabel, I. F., Dijkstra, M., Laurent, P., et al. 2011, A&A, 528, A149
Monreal-Ibero, A., Walsh, J. R., & Vílchez, J. M. 2012, A&A, 544, A60
Motch, C., Pakull, M. W., Soria, R., et al. 2014, Nature, 514, 198
Moustakas, J., Kennicutt, R. C., Jr., Tremonti, C. A., et al. 2010, ApJS, 190, 233-266
Nataf, D. M. 2015, MNRAS, 449, 1171
Oskinova, L. M., Bik, A., Mas-Hesse, J. M., et al. 2019, A&A, 627, A63
Pacucci, F., Mesinger, A., Mineo, S., et al. 2014, MNRAS, 443, 678
Pakull, M. W., Soria, R., & Motch, C. 2010, Nature, 466, 209
Papaderos, P., Guseva, N. G., Izotov, Y. I., et al. 2008, A&A, 491, 113
Park, J., Mesinger, A., Greig, B., et al. 2019, MNRAS, 484, 933
Persic, M., & Rephaeli, Y. 2007, A&A, 463, 481

Pettini, M., & Pagel, B. E. J. 2004, MNRAS, 348, L59 (PP04)
Ponnada, S., Brorby, M., & Kaaret, P. 2020, MNRAS, 491, 3606
Poutanen, J., Fabrika, S., Valeev, A. F., et al. 2013, MNRAS, 432, 506
Prestwich, A. H., Tsantaki, M., Zezas, A., et al. 2013, ApJ, 769, 92
Pustilnik, S. A., Kniazev, A. Y., Pramskij, A. G., et al. 2003, A&A, 409, 917
Ranalli, P., Comastri, A., & Setti, G. 2003, A&A, 399, 39
Reig, P. 2011, Ap&SS, 332, 1
Sacchi, E., Annibali, F., Cignoni, M., et al. 2016, ApJ, 830, 3
Saxena, A., Pentericci, L., Mirabelli, M., et al. 2020, A&A, 636, A47
Schaerer, D., Fragos, T., & Izotov, Y. I. 2019, A&A, 622, L10
Secrest, N. J., Ellison, S. L., Satyapal, S., et al. 2020, MNRAS, doi:10.1093/mnras/staa1692
Senchyna, P., Stark, D. P., Mirocha, J., et al. 2020, MNRAS, 494, 941
Skillman, E. D., Salzer, J. J., Berg, D. A., et al. 2013, AJ, 146, 3
Soria, R., Pakull, M. W., Broderick, J. W., et al. 2010, MNRAS, 409, 541
Soria, R., Long, K. S., Blair, W. P., et al. 2014, Science, 343, 1330
Stasińska, G. 2005, A&A, 434, 507
Sutton, A. D., Roberts, T. P., & Middleton, M. J. 2013, MNRAS, 435, 1758
Svoboda, J., Douna, V., Orlitová, I., et al. 2019, ApJ, 880, 144
Swartz, D. A., Tennant, A. F., & Soria, R. 2009, ApJ, 703, 159
Swartz, D. A., Soria, R., Tennant, A. F., et al. 2011, ApJ, 741, 49
Torrey, P., Vogelsberger, M., Marinacci, F., et al. 2019, MNRAS, 484, 5587
Tzanavaris, P., Fragos, T., Tremmel, M., et al. 2013, ApJ, 774, 136
Tüllmann, R., Gaetz, T. J., Plucinsky, P. P., et al. 2011, ApJS, 193, 31
Tully, R. B., Courtois, H. M., Dolphin, A. E., et al. 2013, AJ, 146, 86
van Zee, L. 2000, ApJL, 543, L31
Walton, D. J., Roberts, T. P., Mateos, S., et al. 2011, MNRAS, 416, 1844
Walton, D. J., Fürst, F., Heida, M., et al. 2018, ApJ, 856, 128
Wang, S., Qiu, Y., Liu, J., et al. 2016, ApJ, 829, 20
Wiktorowicz, G., Sobolewska, M., Lasota, J.-P., et al. 2017, ApJ, 846, 17
Wiktorowicz, G., Lasota, J.-P., Middleton, M., et al. 2019, ApJ, 875, 53
Williams, B. F., Wold, B., Haberl, F., et al. 2015, ApJS, 218, 9
Zampieri, L. & Roberts, T. P. 2009, MNRAS, 400, 677
Zhang, Z., Gilfanov, M., & Bogdán, Á. 2012, A&A, 546, A36
Zibetti, S., Charlot, S., & Rix, H.-W. 2009, MNRAS, 400, 1181

Table A1. X-ray point-source catalog and properties

GALAXY	ID	α_{J2000} (deg)	δ_{J2000} (deg)	θ (arcmin)	N_{FB} (counts)	N_H (10^{22} cm^{-2})	Γ	log F_{FB} (erg cm^{-2} s^{-1})	log L_{FB} (erg s^{-1})	Location Flag
(1)	(2)	(3)	(4)	(5)	(6)–(7)	(8)–(9)	(10)–(11)	(12)	(13)	(14)
NGC0024	1	00 09 44.06	−24 58 16.38	2.9	27.1±5.4	0.021	1.7	−14.2	37.6	3
	2	00 09 44.73	−24 59 03.40	3.0	15.8±4.1	0.021	1.7	−14.5	37.3	3
	3	00 09 45.89	−24 56 00.46	3.0	66.0±9.9	0.194±0.326	1.85±0.77	−13.9	37.9	3
	4	00 09 48.20	−24 58 58.92	2.2	33.0±7.3	0.100±0.322	1.88±0.94	−14.2	37.6	3
	5	00 09 49.87	−24 57 42.08	1.5	7.7±4.3	0.021	1.7	−14.8	37.0	3
	6	00 09 50.25	−25 00 02.24	2.7	5.3±2.4	0.021	1.7	−14.9	36.9	3
	7	00 09 51.27	−24 59 28.45	2.1	9.8±4.6	0.021	1.7	−14.6	37.2	3
	8	00 09 53.62	−24 58 32.01	1.0	36.0±7.5	0.226±0.484	1.68±0.97	−14.1	37.7	1
	9	00 09 54.63	−24 56 57.60	0.9	23.0±6.3	1.657±4.077	0.98±1.76	−14.0	37.8	3
	10	00 09 54.85	−24 57 58.96	0.4	6.6±2.6	0.021	1.7	−14.9	36.9	1
	11	00 09 55.22	−24 57 49.50	0.3	4.6±2.2	0.021	1.7	−15.0	36.8	1
	12	00 09 55.82	−24 59 29.46	1.7	31.9±7.2	0.230±0.413	<2.41	−14.3	37.5	3
	13	00 09 56.19	−24 58 02.13	0.3	13.4±3.7	0.021	1.7	−14.6	37.2	1
	14	00 09 56.27	−24 57 33.72	0.2	24.0±6.4	1.396±0.887	<2.75	−14.3	37.5	1
	15	00 09 56.27	−24 57 57.28	0.2	9.6±3.2	0.021	1.7	−14.7	37.1	1
	16	00 09 57.31	−24 57 42.01	0.2	25.4±5.1	0.021	1.7	−14.3	37.5	1
	17	00 09 58.90	−24 56 57.15	1.0	8.5±3.0	0.021	1.7	−14.8	37.0	1
	18	00 10 00.94	−24 57 27.96	1.0	19.1±5.9	0.021	1.7	−14.5	37.4	3
	19	00 10 03.29	−24 57 30.24	1.6	19.5±5.9	0.021	1.7	−14.4	37.4	3
	20	00 10 03.50	−24 55 28.14	2.8	17.0±5.7	0.021	1.7	−14.5	37.3	3

Note.—The full version of this table contains 2915 sources, including all 1311 sources that were used in our XLF analyses (i.e., Flag=1). An abbreviated version of the table is displayed here to illustrate its form and content. A description of the columns is provided in the Appendix.

APPENDIX

In Table A1, we provide the X-ray point source catalogs, based on the analyses presented in Section 3. The columns include the following: Col.(1): Name of the host galaxy. Col.(2): point-source identification number within the galaxy. Col.(3) and (4): Right ascension and declination of the point source. Col.(5): Offset of the point source with respect to the average aim point of the *Chandra* observations. Col.(6) and (7): 0.5–7 keV net counts (i.e., background subtracted) and 1σ errors. Col.(8)–(9) and (10)–(11): Best-fit column density N_H and photon index Γ, respectively, along with their respective 1σ errors, based on spectral fits to an absorbed power-law model (TBABS$_{Gal}\times$ TBABS $\times$ POW in xspec). For sources with small numbers of counts (<20 net counts), we adopted only Galactic absorption appropriate for each galaxy and a photon index of $\Gamma = 1.7$. Col.(12) and (13): the respective 0.5–8 keV flux and luminosity of the source. Col.(14): Flag indicating the location of the source within the galaxy. Flag=1 indicates the source has $L > 10^{35}$ erg s^{-1}, is within the galactic footprint adopted in Table 1, and is outside a central region of avoidance, if applicable. All XLF calculations are based on Flag=1 sources. Flag=2 indicates that the source is within the adopted galactic footprint, but has a luminosity of $L < 10^{35}$ erg s^{-1}, and was thus excluded from our XLF analysis. Flag=3 indicates that the source is outside the adopted galactic footprint, but within 20% of its outer boundary. These sources are candidates for belonging to the galaxies, but have a high chance of being background objects. Flag=4 indicates that the source is located in the central region of avoidance due to either the presence of an AGN or very high levels of source confusion. Flag=5 indicates that the source is >1.2 times the angular distance to the adopted galactic boundary.